Ultrasonic Wave Propagation in Thick, Layered Composites Containing Degraded Interfaces

by

Peter D. Small

M.S. Operations Research
Columbia University, 2002
B.S. Mechanical Engineering
University of Virginia, 1995

SUBMITTED TO THE DEPARTMENTS OF OCEAN AND MECHANICAL ENGINEERING
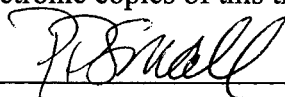IN PARTIAL FULFILLMENT OF THE REQUIREMENTS FOR THE DEGREES OF

NAVAL ENGINEER
AND
MASTER OF SCIENCE IN MECHANICAL ENGINEERING
AT THE
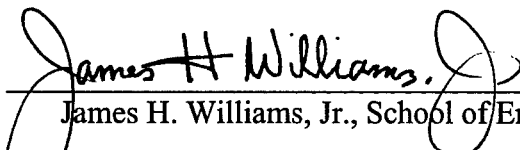MASSACHUSETTS INSTITUTE OF TECHNOLOGY

JUNE 2005

The author hereby grants to MIT and the U.S. Government permission to reproduce and to distribute publicly paper and electronic copies of this thesis document in whole or in part.
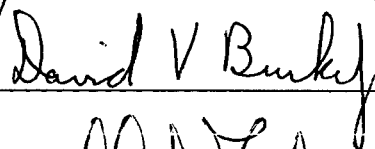
Signature of Author_____

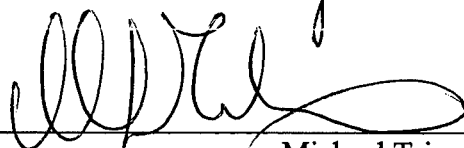Department of Ocean Engineering
May 9, 2005

Certified by _____

James H. Williams, Jr., School of Engineering Professor of Teaching Excellence
Department of Mechanical Engineering
Thesis Supervisor

Certified by _____
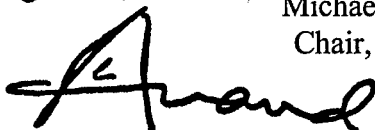
David V. Burke, Senior Lecturer
Department of Ocean Engineering
Thesis Reader

Accepted by _____

Michael Triantafyllou, Professor of Ocean Engineering
Chair, Departmental Committee on Graduate Students
Department of Ocean Engineering

Accepted by _____

Lallit Anand, Professor of Mechanical Engineering
Chair, Departmental Committee on Graduate Students
Department of Mechanical Engineering

20060516059

Page Intentionally Left Blank

Ultrasonic Wave Propagation in Thick, Layered Composites Containing Degraded Interfaces
by
Peter D. Small

Abstract

The ultrasonic wave propagation of thick, layered composites containing degraded bonds is investigated. A theoretical one-dimensional model of three attenuative viscoelastic layers containing two imperfect interfaces is introduced. Elastic material properties and measured values of ultrasonic phase velocity and attenuation are used to represent E-glass and vinyl ester resin fiber-reinforced plastic (FRP) laminate, syntactic foam, and resin putty materials in the model. The ultrasonic phase velocity in all three materials is shown to be essentially constant in the range of 1.0 to 5.0 megahertz (MHz). The attenuation in all three materials is constant or slightly increasing in the range 1.0 to 3.0 MHz. Numerical simulation of the model via the mass-spring-dashpot lattice model reveals the importance of the input signal shape, wave speed, and layer thickness on obtaining non-overlapping, distinct return signals in pulse-echo ultrasonic nondestructive evaluation. The effect of the *interface contact quality* on the reflection and transmission coefficients of degraded interfaces is observed in both the simulated and theoretical results.

Thesis Supervisor: James H. Williams, Jr.
Title: School of Engineering Professor of Teaching Excellence

Thesis Reader: David V. Burke
Title: Senior Lecturer, Department of Ocean Engineering

Page Intentionally Left Blank

Table of Contents

Page Intentionally Left Blank

List of Figures

List of Tables

Page Intentionally Left Blank

Introduction

The United States Navy is increasingly looking to advanced fiber-reinforced plastic (FRP) composites for their unique performance capabilities. In addition to their relatively high specific strength, laminated composites can be integrated with sensor arrays and other materials for enhanced performance and reduced radar signatures. Whereas naval applications of composites have been historically limited to small craft, advances in research, design and construction methods are bringing large composite structures to the Navy's most advanced combatants [1-3]. Nguyen [4] discusses many of the engineering design, fabrication, performance and life cycle support issues that must be addressed in naval applications of composites. Improvements in processing, inspection techniques and maintenance are described by Crane et al. [3].

Reliable and effective nondestructive evaluation (NDE) methods are required for post-fabrication and in service characterization of composite materials. While the field of NDE has matured considerably [5, 6], many of the state-of-the art methods have been developed for thin aircraft composites having fine grain structures. Marine composite laminates tend to be much thicker with coarse fiber reinforcements. These thicker and coarser materials can be highly attenuating, reducing the effectiveness of traditional ultrasonic NDE methods. While other sophisticated inspection techniques including thermography, microwaves, and laser shearography have been applied to marine composite structures [7-12], ultrasonic methods have been shown to be effective in the nondestructive characterization of thick marine composites [13-16].

Problem Statement

A large composite structure proposed for a naval application consists of a monolithic FRP shell with foam-filled hat-shaped stiffeners. The shell and stiffener laminates consist of layers of E-glass woven roving infused with vinyl ester resin via the SCRIMP™ resin transfer molding process. A resin putty is used as an adhesive between syntactic foam blocks and the shell laminate during assembly and as a crack arresting material where the foam blocks meet the shell. The stiffener laminate is bonded to the foam, the resin putty fillet, and the shell via a strong, secondary bond. Figure 1 shows a schematic of a hat-stiffened shell.
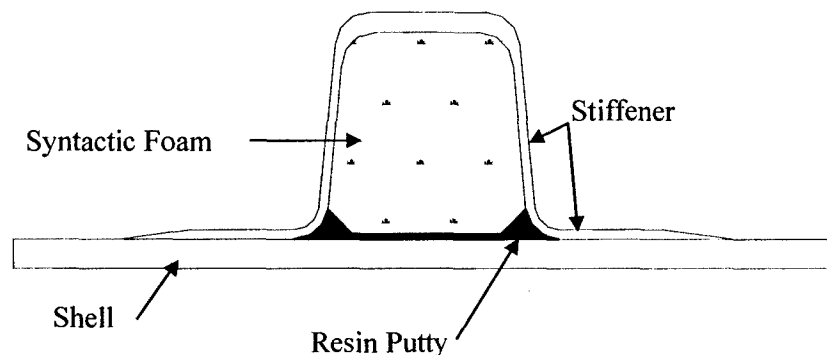
Fig. 1. Schematic of hat-stiffened composite shell.

Post-fabrication NDE of this structure requires inspecting the shell and stiffener laminates for flaws and checking the bond quality of the stiffener to the shell and putty fillet. Flaws might include voids, resin-starved regions, delamination of a layer or layers, or fiber wrinkling in reentrant corners. Finding these flaws is vital for acceptability of the structure and assessment of fatigue response based on initial flaw size. The secondary bond of the stiffener tabbing to the shell is critical to the structural integrity of the stiffened panel under bending loads. The bond between the stiffener and the resin putty fillet is critical to curtail crack

12

propagation from the foam to the joint between the shell and stiffener tabbing. Under bending loads, a crack in this joint could cause separation of the entire stiffener from the shell.

The proposed structure involves a shell laminate thickness on the order of 50 mm, containing numerous layers of coarse-grained cloth reinforcement in the FRP. The features limit the flaw size and depth that can be reliably detected with pulse-echo ultrasonic NDE. The bond between the stiffener tabbing and the shell can be interrogated successfully from the stiffener side because the tabbing thickness is on the order of 12 mm. Assessing the quality of the bond between the stiffener laminate and the resin putty fillet has proved more difficult because of the reentrant corner on the stiffener side, and the laminate thickness from the other side.

It is therefore desirable to understand the wave propagation characteristics of the layered materials within the complex geometry of the hat-stiffened structure in order to improve the ultrasonic inspection of these structures. As an initial investigation, a one-dimensional, theoretical model of layered composite materials containing degraded interfaces is undertaken. A two-dimensional NDE model of the hat-stiffener will be investigated in a future study.

Theoretical Model

One-Dimensional, Three-Layer Material Model

A one-dimensional, three-layer model is the starting point in determining the effects of the material properties, layer thicknesses, and material interface quality on the ultrasonic wave propagation and attenuation in a layered composite structure. This model is particularly applicable to pulse-echo, through-thickness ultrasonic NDE in which a stress wave is applied at the surface and the resulting wave reflections are measured by the same transducer.

Figure 2 shows the three-layer, one-dimensional model. The wave propagation in each layer $j=1,2,3$ is a function of the material mass density ρ_j, attenuation α_j, phase speed c_j, layer

thickness l_j, input signal frequency f, and *interface contact quality* $Q_{k\,k+1}$ k=1,2 (defined later) [17]. The phase speed and attenuation in each layer are assumed to be frequency independent. The material in each layer is represented as a homogeneous, linearly viscoelastic continuum. The constitutive equation for a one-dimensional, viscoelastic solid can be written as [18]

$$\sigma_{11} = \left[\tilde{\lambda}(t) + 2\tilde{\mu}(t)\right] * \dot{\varepsilon}_{11}(t) \tag{1}$$

where σ_{11} is the stress, $\dot{\varepsilon}_{11}(t)$ is the strain rate, $\tilde{\lambda}(t)$ and $\tilde{\mu}(t)$ are relaxation functions analogous to the first and second elastic Lamé constants, and * indicates a convolution integral.
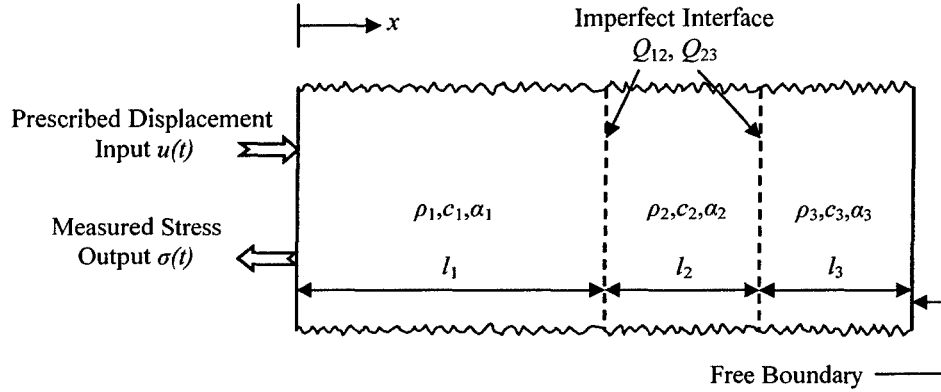
Fig. 2. Three-layer, one-dimensional wave propagation model of materials with mass density ρ, constant phase speed c, constant attenuation α, layer thickness l, and interface contact quality Q.

The boundary condition at x=0 is a prescribed Gaussian-modulated cosinusoidal displacement function $u(x$=0$,t)$

$$u(x = 0,t) = u_p \exp\left[-\frac{1}{2}(2\pi f_\sigma t - 3)^2\right]\cos(2\pi f_c t - 3\frac{f_c}{f_\sigma}) \tag{2}$$

where u_p is the peak magnitude of the input displacement, f_c is the central cyclic frequency, and f_σ is the cyclic frequency standard deviation. The input signal is applied at time t=0 and the

input surface is then rigidly fixed for all time thereafter. The exposed surface of the last layer at

$x = l_1 + l_2 + l_3$ is a free surface.

The concept of an imperfect interface between layered materials is introduced to model

degraded bonds or delaminations between layers. A contact quality Q is assigned to each

interface between adjacent layered materials. The value of Q ranges between $Q=1$ (perfect

bonding between layers) and $Q=0$ (complete delamination or a free surface.) The value of Q

affects the contact force between adjacent particles across a material interface and is related to

the bond quality between the two layers [17]. The reflection and transmission coefficients of an

ultrasonic stress wave at a material interface are then functions of both the material properties on

either side of the interface and the interface contact quality.

The time history of stress at the surface $\sigma_0 = \sigma(x = 0, t)$ will be taken as a pulse-echo

ultrasonic NDE representation output.

Parameterization

In order to remove the effect of the (arbitrary) peak magnitude of the input signal u_p on σ_0,

the surface stress can be expressed as

$$\frac{\sigma_0}{u_p} = function\left(f_c, f_\sigma, l_1, l_2, l_3, c_1, c_2, c_3, \rho_1, \rho_2, \rho_3, \alpha_1, \alpha_2, \alpha_3, Q_{12}, Q_{23}, t\right) \tag{3}$$

This form of the surface stress can be expressed in terms of the following dimensionless

parameters:

$$\frac{\sigma_0 \lambda_1}{u_p \rho_1 c_1^2} = function\left(\frac{f_\sigma}{f_c}, \frac{\rho_2}{\rho_1}, \frac{\rho_3}{\rho_1}, \frac{c_2}{c_1}, \frac{c_3}{c_1}, \frac{k_1}{2\alpha_1}, \frac{k_2}{2\alpha_2}, \frac{k_3}{2\alpha_3}, \frac{l_1}{\lambda_1}, \frac{l_2}{\lambda_2}, \frac{l_3}{\lambda_3}, Q_{12}, Q_{23}, \frac{c_1 t}{2l_1}\right) \tag{4}$$

15

where k_j and λ_j are the wavenumber and wavelength in layer j corresponding to the center frequency.

$$k_j = \frac{2\pi f_c}{c_j} = \frac{2\pi}{\lambda_j}$$ (5)

The parameter $\dfrac{k_j}{2\alpha_j}$ is the number of wavelengths in material j required to attenuate the wave amplitude to $e^{-\pi}$, or roughly 4% of the original value where amplitude is of the form $\sigma(x) = \sigma_0 e^{(-\alpha x)}$. It is analogous to a measure of the energy loss mechanisms in solids called the quality factor*, which relates the amount of energy dissipated in the system to the stored elastic energy. Detailed discussion about the quality factor is included in Appendix A. The parameter $\dfrac{l_j}{\lambda_j}$ is a ratio of the layer thickness to the wavelength in material j at center frequency f_c. The parameter $\dfrac{c_1 t}{2l_1}$ is the time divided by the characteristic time required for the first reflection from the first material interface to arrive back at the input surface ($x=0$). The dimensionless surface stress $\dfrac{\sigma_0 \lambda_1}{\rho_1 c_1^2 u_p}$ is the ratio of the surface stress to the stress in a one-dimensional solid of length λ_1 and modulus $\rho_1 c_1^2$ subjected to a prescribed displacement u_p.

Numerical Discretization

Mass-Spring-Dashpot Lattice Model

The mass-spring-dashpot lattice model (MSDLM) of Thomas et al. [19] was modified to investigate the wave propagation and attenuation of layered composite materials. This model

---

* The quality factor as described is commonly represented in the literature by the symbol Q. This paper uses Q to represent the imperfect interface contact quality.

expands the mass-spring lattice model (MSLM) of Yim and Sohn [20] and Yim and Choi [21] in order to better model the viscoelastic and attenuating nature of composite materials. The MSDLM discretizes a viscoelastic continuum into an assemblage of particles interconnected by standard linear elements as shown in Fig. 3.
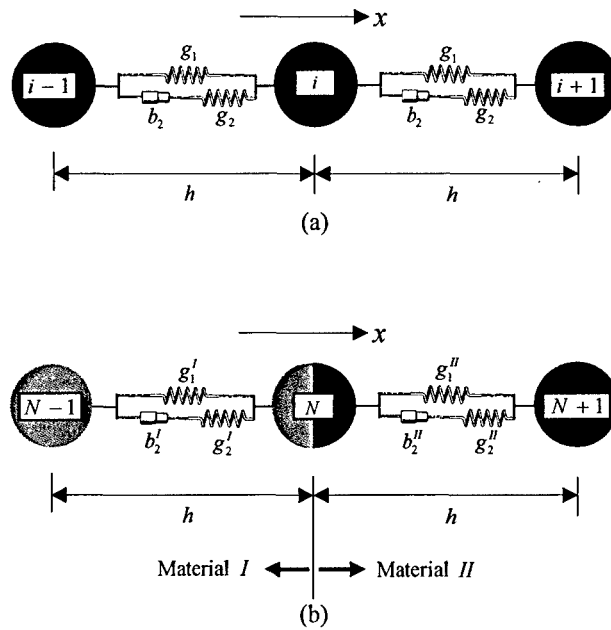
Fig. 3. Schematics of MSDLM discretization in vicinity of (a) interior particle at position i and (b) particle at interface of dissimilar materials at position N where h is grid spacing, and various g and b are respective spring constants and dashpot coeffiecients related to governing partial differential equations of each standard linear solid [19].

The various spring constants and dashpot coefficients are related to the exact partial differential equations governing a one-dimensional standard linear solid. The particle displacements, particle velocities, and volumetric forces through each standard linear element are numerically integrated with an explicit, fourth-order Runge Kutta algorithm. The force per unit volume $f(x,t)$ between particles i and $i+1$ is then related to the stress $\sigma(x,t)$ between particles by

$$\sigma(x,t) = f(x,t) \cdot h \qquad (6)$$

where h is the spacing between particles. The MSDLM has been shown to give good agreement with analytical solutions for steady-state and transient analyses [19].

The phase speed and attenuation of the viscoelastic materials in the three-layer model are assumed to be frequency independent. Constant phase speed and attenuation can be accurately modeled in the MSDLM when [0]

$$\frac{k}{2\alpha} \geq 5 \qquad (7)$$

To ensure stability and convergence of the Runge-Kutta integration algorithm, the numerical integration time step Δt must satisfy both

$$C \equiv \frac{c_{max}\Delta t}{h} \leq 1.30 \qquad (8)$$

$$\frac{\Delta t}{\tau} \leq 2.78 \qquad (9)$$

where C is the maximum Courant number, c_{max} is the maximum phase speed in the layered media, h is the spacing between particles in the grid, and τ is the relaxation time of the standard linear solid. To reduce the numerical phase and dissipation error to less than 1% of the corresponding analytical values, the grid spacing must be at most $1/20^{th}$ of the smallest wavelength present in the layered media. To obtain smoother waveforms for analysis, the grid spacing is further reduced to $1/40^{th}$ of the smallest wavelength λ_{min}

$$h = \frac{\lambda_{min}}{40} = \frac{\pi c_{min}}{20\omega_{max}} \qquad (10)$$

where c_{min} is the minimum phase speed in the layered media and ω_{max} is the maximum angular frequency in the frequency spectrum [19]

$$\omega_{max} = \omega_c + 3\omega_\sigma \qquad (11)$$

$$\omega_\sigma = 2\pi f_\sigma \qquad (12)$$

Implementation of Imperfect Interface

The modeling of an imperfect interface between composite layers follows the local interaction simulation approach (LISA) of Delsanto and Scalerandi [17]. This formulation allows for the modeling of delaminations or degraded bonds between adjacent composite layers. Consider the interface of two dissimilar materials at particle N located at $x= \xi$ as shown in Fig. 4. The volumetric contact force f_{ct} between half particles at the interface can be shown to be [Appendix C]

$$f_{ct} = Q\left(\frac{\rho_I f_{N+\frac{1}{2}} + \rho_{II} f_{N-\frac{1}{2}}}{\rho_I + \rho_{II}} \right) \qquad (13)$$

where $f_{N-1/2}$ and $f_{N+1/2}$ are the forces from the adjacent particles in the grid and ρ_I and ρ_{II} are the densities of the materials on either side of the interface. Q is the interface contact quality and has values ranging from $Q=0$ (no contact force between particles) to $Q=1$ (perfect contact).

19
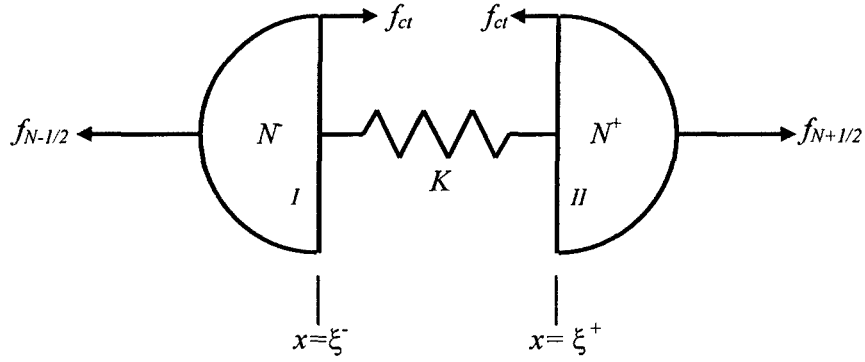
Fig. 4. Imperfect interface between materials *I* and *II* at particle *N*, at $x = \xi$, where *K* is interfacial stiffness, f_{ct} is contact force, and $f_{N-1/2}$ and $f_{N+1/2}$ are forces from adjacent particles in grid.

This formulation retains the continuity of stress across the interface, but allows the displacements of the adjacent half-particles at the interface to differ. The stress and displacement boundary conditions can be written as [22]

$$\frac{1}{2}\left[\sigma(\xi^+) + \sigma(\xi^-)\right] \approx K\left[u(\xi^+) - u(\xi^-)\right] \tag{14}$$

$$\sigma(\xi^+) - \sigma(\xi^-) = 0 \tag{15}$$

K is an interfacial stiffness per unit area and can be thought of as the spring constant of a distributed massless spring between the two half-particles at the interface. For an incident longitudinal wave of frequency ω at the interface it can be shown that [Appendix C]

$$K = \frac{h\omega^2}{2}\left(\frac{\rho_I \rho_{II}}{\rho_I + \rho_{II}}\right)\left(\frac{Q}{Q-1}\right) \tag{16}$$

As the interface contact quality $Q \to 0$, the stiffness $K \to 0$ and there is no connection (or force transmitted) between particles. As $Q \to 1$, the stiffness $K \to \infty$, and the particles at the interface are rigidly connected.

The transmission and reflection coefficients of the degraded interface can be derived as a function of K in a similar fashion. Using conservation of energy at the interface with an incident, reflected, and transmitted longitudinal wave, the transmission and reflection coefficients of the interface can be shown to be [Appendix C]

$$T = \frac{\dfrac{2Z_I}{Z_I + Z_{II}}}{1 - \dfrac{i\omega}{K}\dfrac{Z_I Z_{II}}{Z_I + Z_{II}}} \tag{17}$$

$$R = \frac{\dfrac{Z_I - Z_{II}}{Z_I + Z_{II}} - \dfrac{i\omega}{K}\dfrac{Z_I Z_{II}}{Z_I + Z_{II}}}{1 - \dfrac{i\omega}{K}\dfrac{Z_I Z_{II}}{Z_I + Z_{II}}} \tag{18}$$

The Z coefficients are the elastic impedances of each material [23]

$$Z = \rho c \tag{19}$$

When $Q \rightarrow 1$ and $K \rightarrow \infty$, the transmission and reflection coefficients for a perfect boundary are

$$T_{perfect} = \frac{2Z_I}{Z_I + Z_{II}} \tag{20}$$

$$R_{perfect} = \frac{Z_I - Z_{II}}{Z_I + Z_{II}} \tag{21}$$

When $Q \rightarrow 0$ and $K \rightarrow 0$, the transmission and reflection coefficients for a free surface are

$$T_{freesurface} = 0 \tag{22}$$

$$R_{freesurface} = 1 \tag{23}$$

Figure 5 shows the magnitudes of the reflection and transmission coefficients for two identical (equal impedance) half-spaces across an interface of varying contact quality.
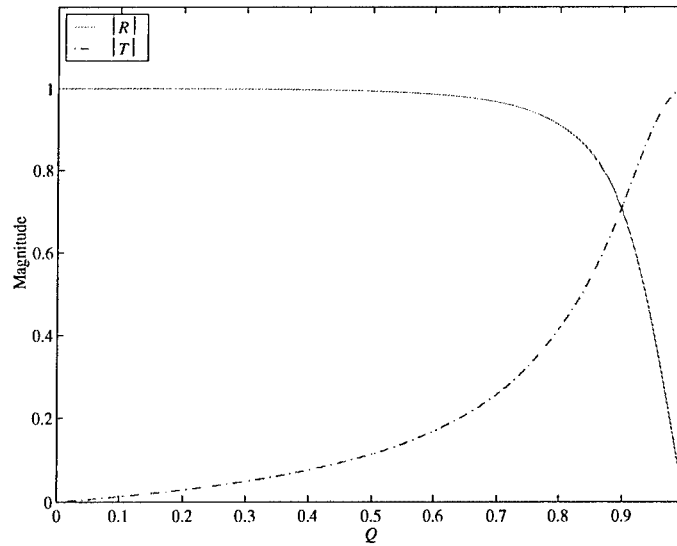
Fig. 5. Magnitudes of reflection and transmission coefficients, R and T, of two identical half spaces with c=2750 m/s, ρ=1882 kg/m^3, f=2.0 MHz, h=0.0001 m as a function of interface contact quality Q.

Materials Constitutive Data

Materials

The reinforcing fibers of the FRP shell and stiffener laminates consist of layers of 0.814 kg/m^2 E-glass cloth woven in a 3x1 twill pattern. The laminate schedule is a repeating pattern of [0°/±45°/90°]$_s$ oriented plies stacked to achieve the total thickness. The layers of reinforcing fibers are infused with DERAKANE® 8084 vinyl ester resin with rubber toughening agents added via the SCRIMP™ resin-infusion process. The fiber content of the cured laminate is nominally 52%-55% by volume [24]. The nominal cured ply thickness is 0.61mm and the cured laminate density is 1882 kg/m^3.

The syntactic foam is comprised of 3M™ Scotchlite™ K25 Glass Bubbles suspended in an unspecified epoxy resin matrix. The mean diameter of the glass microspheres is

0.55 microns. The foam density is 512 kg/m^3 and the microsphere content is approximately 70% by mass. The resin putty is a particulate-toughened DERAKANE$^®$ 8084 vinyl ester resin with a density of 1245 kg/ m^3.

This information was provided by the material supplier. In order to accurately model the behavior of these materials and generate the parameters of Eq. (5), however, ultrasonic phase speed and attenuation data were required.

Test Specimens and Data Acquisition

Cube-shaped samples of each material were obtained in order to measure the phase speed and attenuation properties over a range of frequencies for input to the MSDLM model. The number of samples and nominal size of each are listed in Table 1. The faces of the FRP cubes were machine polished in order to reduce the variability in ultrasonic measurements caused by the rough, bag-side finish of the laminate. Photographs of the samples can be seen in Appendix D.

Table 1. Test specimen summary.

Material	Number of Cubes	Nominal Edge Length
FRP	2	1.42 cm
FRP	2	5.08 cm
Syntactic Foam	1	2.54 cm
Syntactic Foam	1	5.08 cm
Syntactic Foam	1	7.62 cm
Resin Putty	1	2.54 cm
Resin Putty	1	5.08 cm
Resin Putty	1	7.62 cm

All ultrasonic measurements were taken with a PANAMETRICS-NDT^{TM} EPOCH 4 flaw detector in the through-transmission mode and K B-Aerotech type Alpha, 5 MHz, 1.27cm

diameter, hard-faced transducers. Water was used as a couplant between the transducer and specimen for all measurements.

Velocity measurements were obtained directly with the flaw detector. In order to calculate attenuation, the ultrasonic through-transmission output signal amplitudes (A_1, A_2) of two otherwise identical specimens of differing lengths (l_1, l_2; $l_2 > l_1$) were obtained at a given input frequency ω. The attenuation $\alpha(\omega)$ was then calculated by [25]

$$\alpha(\omega) = \frac{\ln(A_1/A_2)}{l_2 - l_1}$$

(24)

where ln is the natural logarithm. With three differently sized cubes of resin putty and syntactic foam, the attenuation can be calculated using three different combinations of two sizes. With two each of two sizes of FRP cubes, the attenuation can be calculated with four different combinations of two sizes.

The cubic samples enabled velocity measurements and attenuation calculations for each sample in three orthogonal directions. Each axis of each cube was labeled as 1, 2, or 3. Figure 6 shows the orientation of the coordinate axes for the FRP laminate. The 1 direction is perpendicular to the plane of the plies, and represents the direction of interest for the one-dimensional, through-thickness NDE represented by the MSDLM model. Test velocity measurements showed the resin putty and syntactic foam to be relatively isotropic materials, so formal data were only subsequently collected from the (arbitrarily selected) 1 direction. As expected, the FRP was approximately transversely isotropic and data were collected from all three axes.
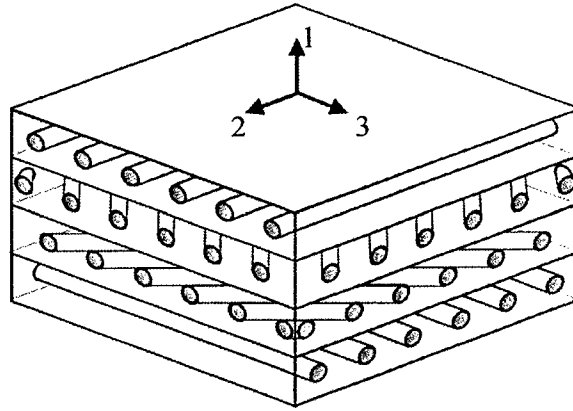
Fig. 6. Coordinate axes for FRP test specimens.

Results

Ultrasonic phase velocity and attenuation measurements were taken over the range of frequencies from 0.1 to 5.0 megahertz (MHz). The complete data and more details can be found in Appendix D. The ultrasonic phase velocity in each material was approximately constant over the frequency range. The attenuation in each material was constant or increased slightly with increasing frequency in the range 1.0-3.0 MHz.

The ultrasonic phase velocity measurements in the FRP material are plotted in Fig. 7. Each data point represents the mean of the measurements of the four FRP blocks at that frequency. The height of the error bar at each data point is equal to one standard deviation s as calculated by

$$s = \sqrt{\frac{n\sum x_i - \left(\sum x_i\right)^2}{n^2}} \tag{25}$$

where n is the number of samples and x_i are the individual measurements $i=1,2,\dots,n$. The average ultrasonic phase velocity in FRP axes 2 and 3 are similar and greater than that of FRP axis 1. Despite having very different constitutions, the syntactic foam and resin putty have almost identical ultrasonic phase velocities, as shown in Fig. 8.
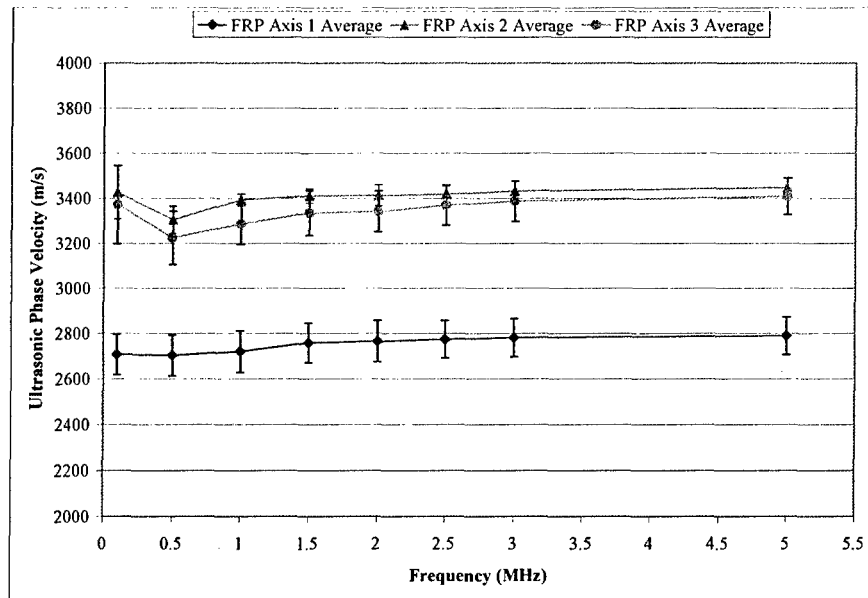
Fig. 7. FRP average ultrasonic phase velocity. Each data point represents the mean of measurements from four samples at that frequency. The total height of the error bar represents one standard deviation for those four points.
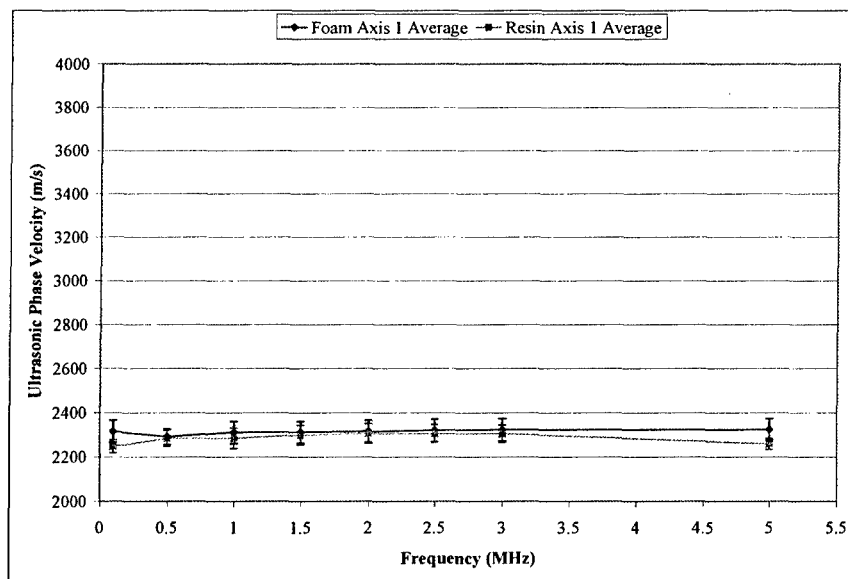
Fig. 8. Syntactic foam and resin putty average ultrasonic phase velocity. Each data point represents the mean of measurements from three samples at that frequency. The total height of the error bar represents one standard deviation for those three points

An unexpected dip in velocity at low frequencies can be seen in FRP axes 2 and 3 and the syntactic foam. This unexplained behavior was seen sporadically in all three materials throughout multiple data collection events with different transducers. One possible source of this behavior is interaction between the wavelength of the ultrasonic signal at low frequency and the thickness of the sample. At 0.1 MHz in a 2.54 cm sample, the ratio $\dfrac{l}{\lambda}$ is on the order of 1.0 for these materials, where l is the sample thickness and λ is the wavelength. The trend was not seen consistently, however, and in some cases was more prominent in larger samples [Appendix D]. Regardless of the source of this low frequency behavior, the ultrasonic phase velocity of all three materials is essentially constant above 1.0 MHz. This constant value was estimated by calculating a global average of the measured velocities at all frequencies within a material and axis.

As a basis of comparison for the global average of ultrasonic phase velocity in each sample, the theoretical phase velocity of a longitudinal wave in an infinite, elastic, isotropic solid was calculated [26]

$$c_{theoretical} = \sqrt{\frac{\lambda + 2\mu}{\rho}} \qquad (26)$$

where c is phase velocity, ρ is density. λ and μ are the first and second Lamé constants as calculated by [27]

$$\lambda = \frac{E\nu}{(1+\nu)(1-2\nu)} \qquad (27)$$

$$\mu = \frac{E}{2(1+\nu)} \qquad (28)$$

where E is the modulus of elasticity and v is Poisson's ratio. The theoretical phase velocities were calculated using representative values of E, v, and ρ provided with the material samples. These representative elastic material data do not represent actual values of the specific lots of material from which the samples were gathered. Table 2 shows both the theoretical and global average velocities for each material. The global averages were within 12% of the calculated theoretical values for all three axes of the FRP and the syntactic foam, but the global average of the resin putty phase velocity was significantly higher than the theoretical value. In addition to the fact that the theoretical results assume elastic and isotropic materials, slight variations in batches of each material may cause the elastic properties of the actual samples to differ from the representative values provided.

Table 2. Theoretical and measured average phase velocity.

Parameter	FRP Axis 1	FRP Axis 2	FRP Axis 3	Syntactic Foam	Resin Putty
Density ρ (kg/m^3)	1882	1882	1882	512	1245
Modulus of Elasticity E (GPa)	10.4	24.1	24.1	2.2	3.1
Poisson's Ratio v	0.314	0.135	0.099	0.350	0.300
First Lamé Constant λ (GPa)	6.7	3.9	2.7	1.9	1.8
Second Lamé Constant μ (GPa)	4.0	10.6	11.0	0.8	1.2
Theoretical Phase Velocity $c_{theoretical}$ (m/s)	2785	3656	3618	2626	1831
Global Average Phase Velocity (m/s)	2750	3406	3341	2309	2290
% Difference	1%	7%	8%	12%	-25%

The attenuation of each material at each frequency was calculated using Eq. (24). The average values of the four possible FRP attenuation calculations at each frequency are plotted in Fig. 9.
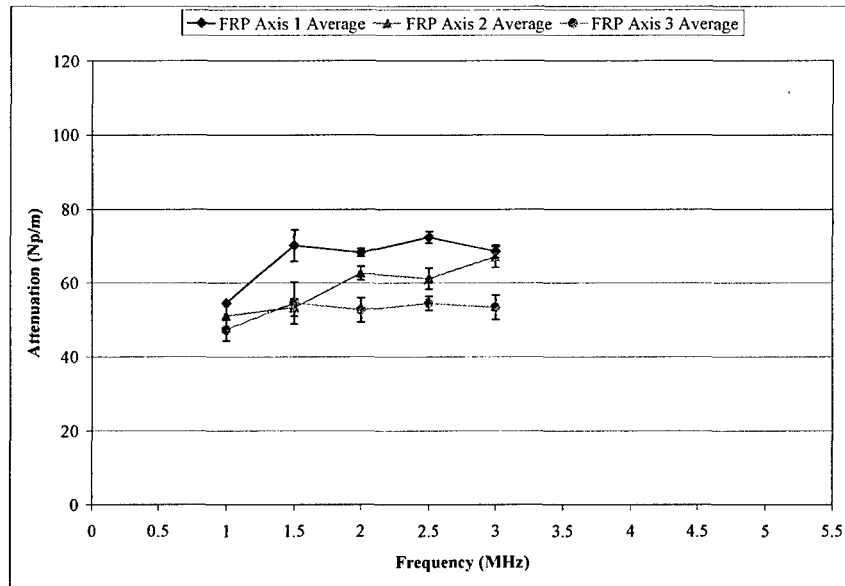
Fig. 9. FRP attenuation average values. Points on the solid lines represent the mean of four data points in that axis at that frequency. The height of the error bar represents one standard deviation for those four points.

While the plots of attenuation data are not as smooth as the phase velocity plots, several trends can be seen in the FRP material. The attenuation values in axes 2 and 3 (in the plane of the plies) are similar and slightly less those in axis 1 (through the plies). The difference in attenuation between axes, however, is less than the difference seen in the velocity data. Data points taken below 1.0 and above 3.0 MHz were erratic and were not used in average value calculations. The attenuation calculations for the syntactic foam and resin putty are plotted in Fig. 10. Each point on the graph is the average value of three attenuation calculations from the three differently sized samples. Again, the low frequency data were erratic and were omitted.

29
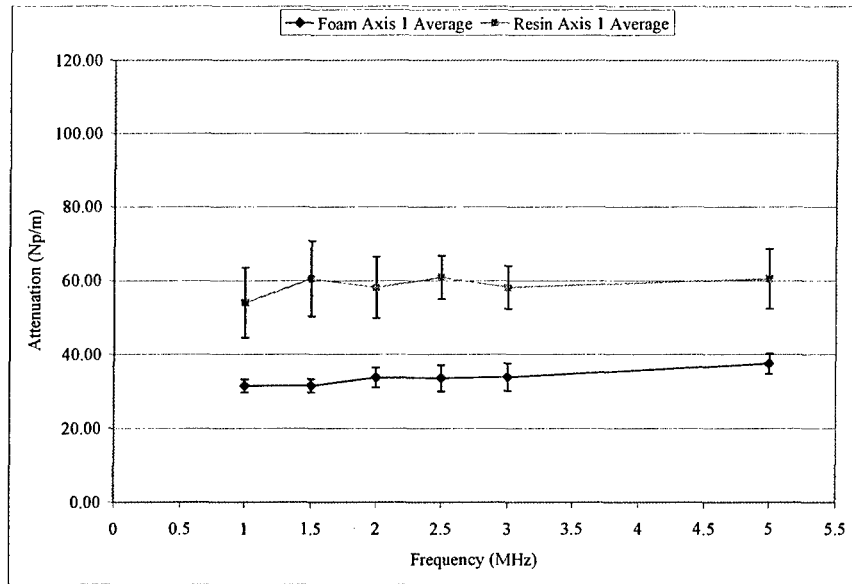
Fig. 10. Syntactic foam and resin putty axis 1 attenuation average values. Points on the solid line represent the mean of three data points at that frequency. The height of the error bar represents one standard deviation for those three points.

The attenuation values of the FRP and resin putty were similar. Unexpectedly, the syntactic foam displayed the lowest attenuation of the three materials. From 1.0 to 3.0 MHz the attenuation was constant or slightly increasing with increasing frequency in all three materials. This indicates that the assumption of constant attenuation used in the formulation of the three-layer model is reasonable. Similar to the procedure used with the velocity data, a global average attenuation value was calculated for each material (and axis for FRP). The global average velocities and attenuation values can be seen in Table 3. The standard deviation values in Table 3 are calculated with Eq. (25) using all data points for each material.

Table 3. Global average and standard deviation of ultrasonic phase velocity and attenuation measurements for three materials.

Material	Global Average Ultrasonic Phase Velocity (m/s)	Velocity Standard Deviation (m/s)	Global Average Attenuation (Np/m)	Attenuation Standard Deviation (Np/m)
FRP Axis 1	2750	177	68.2	7.3
FRP Axis 2	3406	123	59.1	8.1
FRP Axis 3	3341	223	52.5	7.8
Syntactic Foam	2309	98	33.6	6.0
Resin Putty	2290	82	58.7	16.4

Implementation of the Three-Layer Model

Dimensionless Parameters

The global average values of attenuation and phase velocity are used to generate the non-dimensional parameters of Eq. (5). The results are seen in Table 4. The configuration of the layers consists of FRP in the first layer, resin putty in the second layer, and syntactic foam in the third layer. The thickness of each layer is 1.27 cm. Based on the analysis of input signal shape discussed in the next section, an input signal with f_c=2.0 MHz and $\dfrac{f_\sigma}{f_c} = 0.3$ is selected for this example.

Table 4. Non-dimensional parameters for input to three-layer model.

Parameter	f_σ/f_c	ρ_2/ρ_1	ρ_3/ρ_1	c_2/c_1	c_3/c_1	Q_{12}	Q_{23}
Value	0.30	0.66	0.27	0.83	0.84	Varies	Varies
Parameter	$k_1/2\alpha_1$	$k_2/2\alpha_2$	$k_3/2\alpha_3$	l_1/λ_1	l_2/λ_2	l_3/λ_3	
Value	33.5	46.8	80.8	9.24	11.11	10.98	

Input Signal Shape

The analysis of the three-layer model simulation is based on finding and comparing the peaks of the reflected signals that are seen in the time history of surface stress. The primary signals of interest are the first reflection from the first interface and the first reflection from the second interface. While the first reflection from the first interface is clearly discernable, the first reflection from the second interface is easily confused with multiple reflections in the first and second layers. The factors that most affect this interference are the shape of the input signal and the ratios of the wave speeds and layer thicknesses between layers.

Figure 11 shows the wave propagation as a function of depth and time in the three layers in the configuration described above. The reflections of interest are shown with solid lines, while other reflections are shown with dotted lines.
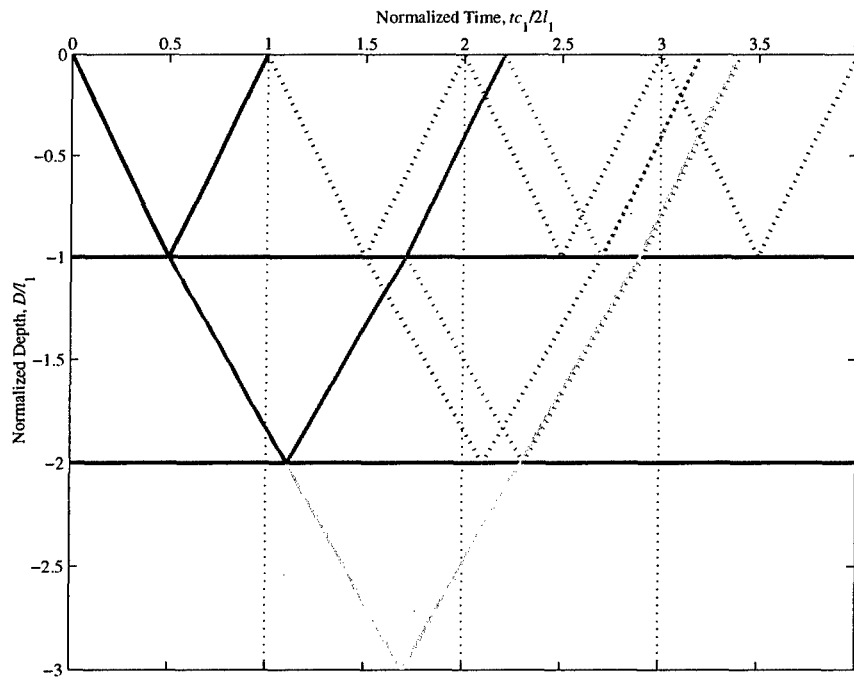
Fig. 11. Wave propagation in three layer composite with c_1=2750 m/s, l_1=0.0127 m, c_2/c_1=0.83, c_3/c_1=0.84, l_2/l_1=1.0, l_3/l_1=1.0. Only reflections that arrive back at surface at or before $tc_1/2l_1$=4 are shown.

32

For this combination of layer thicknesses and wave speeds, the first reflection from the second interface arrives back at the surface shortly after the second reflection from the first interface does. Depending on the shape of the input signal, these two signals can easily overlap and confuse the interpretation of the time history of surface stress. The back wall reflection is almost sure to be distorted by multiple reflections from both interfaces. Since making an assessment of the interface contact quality is of primary concern in this study, no attempt is made to identify or quantify the back wall return in the time history of surface stress.

To better isolate the first reflection from the second interface in the time history of surface stress, the shape of the input signal can be altered. The narrower the input signal (and resulting reflections) in the time domain, the easier it is to discern reflections of interest from other reflections. The bandwidth of the input signal dictates the width of the reflections seen at the surface. In this formulation, the bandwidth of the Gaussian-modulated cosinusoidal input function of Eq. (2) is represented by the non-dimensional parameter $\frac{f_\sigma}{f_c}$. A large value of $\frac{f_\sigma}{f_c}$ will result in a narrow signal in the time domain. The effect of increasing the bandwidth on the width of the input signal can be seen in Fig. 12.
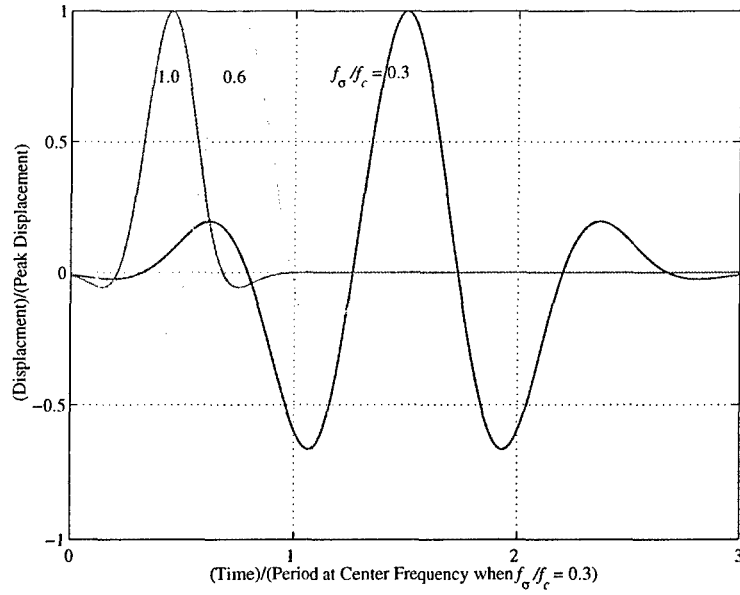
Fig. 12. Effect of bandwidth f_σ/f_c on width of Gaussian-modulated cosinusoidal input displacement function.

By assuming that the width of the Gaussian-modulated input signal is equal to six temporal standard deviations, a minimum bandwidth to separate the second reflection from the first interface and the first reflection from the second interface can be calculated [0].

$$\frac{f_\sigma}{f_c} > \frac{1}{f_c} \cdot \frac{3}{\pi} \cdot \frac{c_1}{2l_1} \cdot \left| -1 + \frac{l_2/l_1}{c_2/c_1} \right|^{-1} \tag{29}$$

This equation is valid for the specific case of interference between the first reflection from the second interface and the second reflection from the first interface. Figure 13 shows Eq. (29) plotted for a range of frequencies and normalized layer thickness, $\dfrac{l_2/l_1}{c_2/c_1}$. This plot is used to determine the bandwidth settings for each possible layer configuration and input frequency. For

the case with f_c=2.0 MHz, c_1=2750 m/s, l_1=0.0127 m, and $\dfrac{l_2/l_1}{c_2/c_1} = 1.2$, a bandwidth $\dfrac{f_\sigma}{f_c} \geq 0.25$ is

required to separate the first reflection from the second interface and the second reflection from

the first interface. The dashed lines in Fig. 13 represent this case.
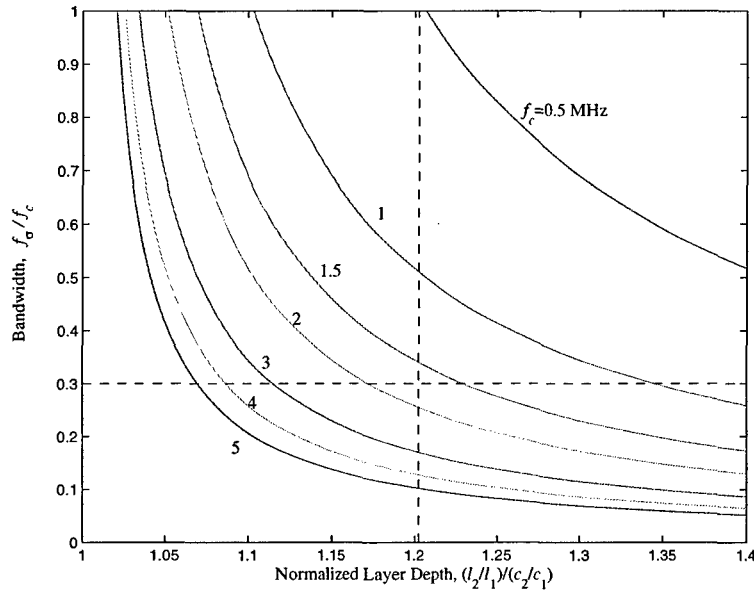
Fig. 13. Minimum bandwidth required to prevent overlap in first reflection from second interface and second reflection from first interface when c_1=2750 m/s and l_1=0.0127 m.

Results

The first reflection from the first interface is the key in assessing the bond quality of the

first interface. This reflection is unaffected by the condition of the second interface or the

material properties of the third layer. Figure 14 shows the shape of this first reflection plotted for

several values of interface contact quality Q_{12}. The peak value of each reflection is marked with

an "x". The amplitude and phase information from these peaks is used to calculate effective

values of the magnitude $|R_{12}|$ and phase angle Φ_{12} of the first interface reflection coefficient R_{12}.
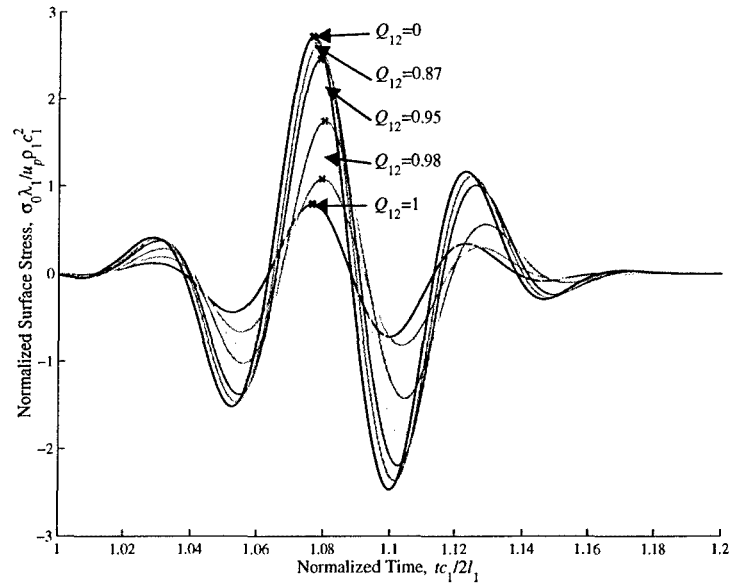
Fig. 14. First reflection seen at the surface from the first interface. f_c=2.0 MHz, f_a/f_c=0.3, c_1=2750 m/s, l_1=0.0127 m, ρ_1=1882 kg/m^3, c_2/c_1=0.83, ρ_2/ρ_1=0.66.

The largest peak is seen when Q_{12}=0 and no energy is transmitted through the interface (see Eq. (23)). Assuming $|R_{12}| = 1$ when Q_{12}=0, $|R_{12}|$ at each value of Q_{12} is calculated by dividing each peak reflection magnitude by the peak reflection magnitude at Q_{12}=0. These calculated reflection coefficient magnitudes and the theoretical values from Eq. (18) are plotted in Fig. 15. The calculated values from the MSDLM results agree closely with the theoretical values. As predicted by Fig. 14, $|R_{12}|$ remains near one for values of Q_{12} up to 0.8 and then drops sharply thereafter.
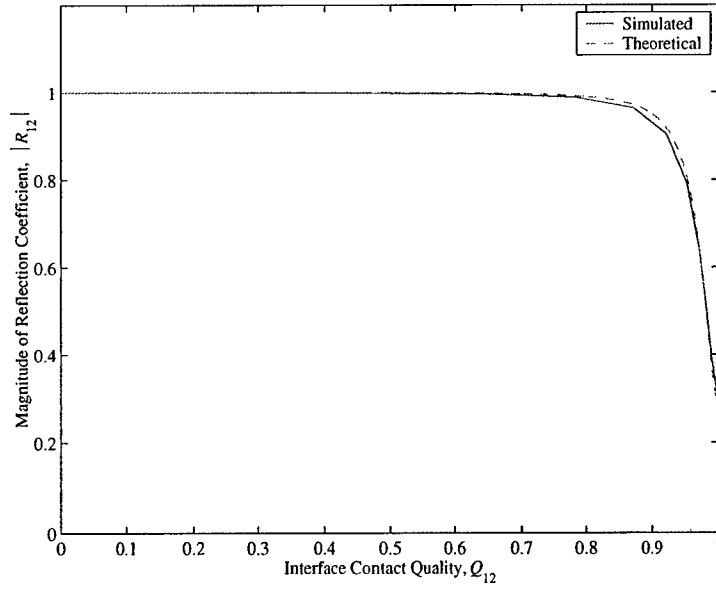
Fig. 15. Magnitude of simulated and theoretical reflection coefficients of the first interface with f_c=2.0 MHz, f_o/f_c=0.3, c_1=2750 m/s, l_1=0.0127 m, ρ_1=1882 kg/m^3, c_2/c_1=0.83, ρ_2/ρ_1=0.66.

The phase angle of the first interface reflection coefficient Φ_{12} is be calculated in a similar fashion. The time of occurrence of each peak reflection magnitude is subtracted from that of the peak magnitude at Q_{12}=0 and the result is converted into degrees. These results are plotted with the theoretical value of the phase angle of R_{12} (from Eq. (18)) in Fig. 16. Again the calculated values from the MSDLM algorithm closely agree with the theoretical values. The curve in Fig. 16 is somewhat jagged as a result of the spacing of the Q_{12} data points and the grid spacing in the MSDLM algorithm.
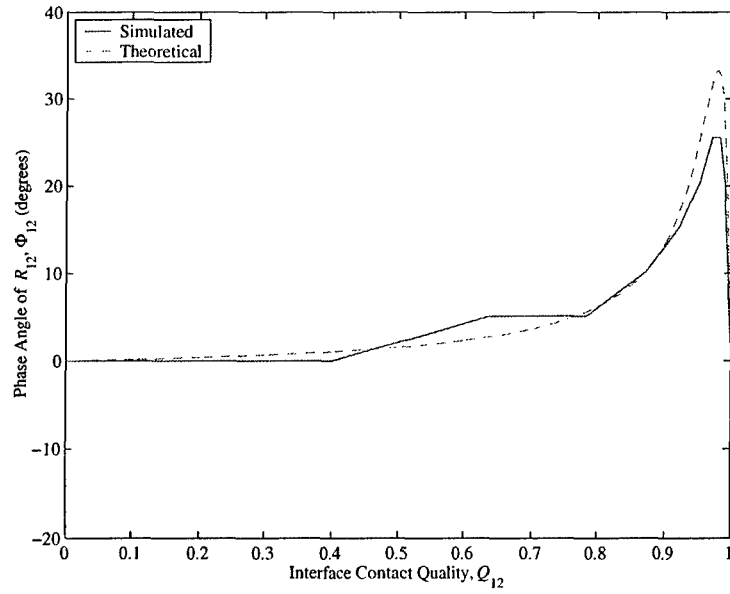
Fig. 16. Simulated and theoretical phase angles of the reflection coefficient of the first interface for f_c=2.0 MHz, f_d/f_c=0.3, c_1=2750 m/s, l_1=0.0127 m, ρ_1=1882 kg/m³, c_2/c_1=0.83, ρ_2/ρ_1=0.66.

Similar results are seen for the first reflection from the second interface. In this case, however, the signal seen at the surface is a function of the transmission coefficient of the first interface T_{12} (on both the outgoing and return trips) and the reflection coefficient of the second interface R_{23}. The theoretical magnitudes and phase angles of $T_{12}{}^2R_{23}$ are calculated using Eqs. (16)-(19). The comparison of the results from the three-layer model simulation with the theoretical results is less straightforward than before, however. The maximum amplitude seen in the first reflection from the second interface is when Q_{12}=1 (maximum signal transmitted) and Q_{23}=0 (maximum signal reflected). The magnitudes of the peak surface stress from the three-layer model simulation as Q_{12} and Q_{23} vary are normalized by the peak surface stress when Q_{12}=1 and Q_{23}=0. Similarly, the theoretical values of $\left|T_{12}^2 R_{23}\right|$ are normalized by the value of $\left|T_{12}^2 R_{23}\right|$ when Q_{12}=1 and Q_{23}=0. These normalized simulated and theoretical results are seen in

Fig. 17 and Fig. 18. In Fig. 17, as Q_{23} varies, the curves follow the shape of R_{23} just as in Fig. 5

and Fig. 15. In Fig. 18, as Q_{12} varies, the curves follow the shape of $T_{12}{}^2$.
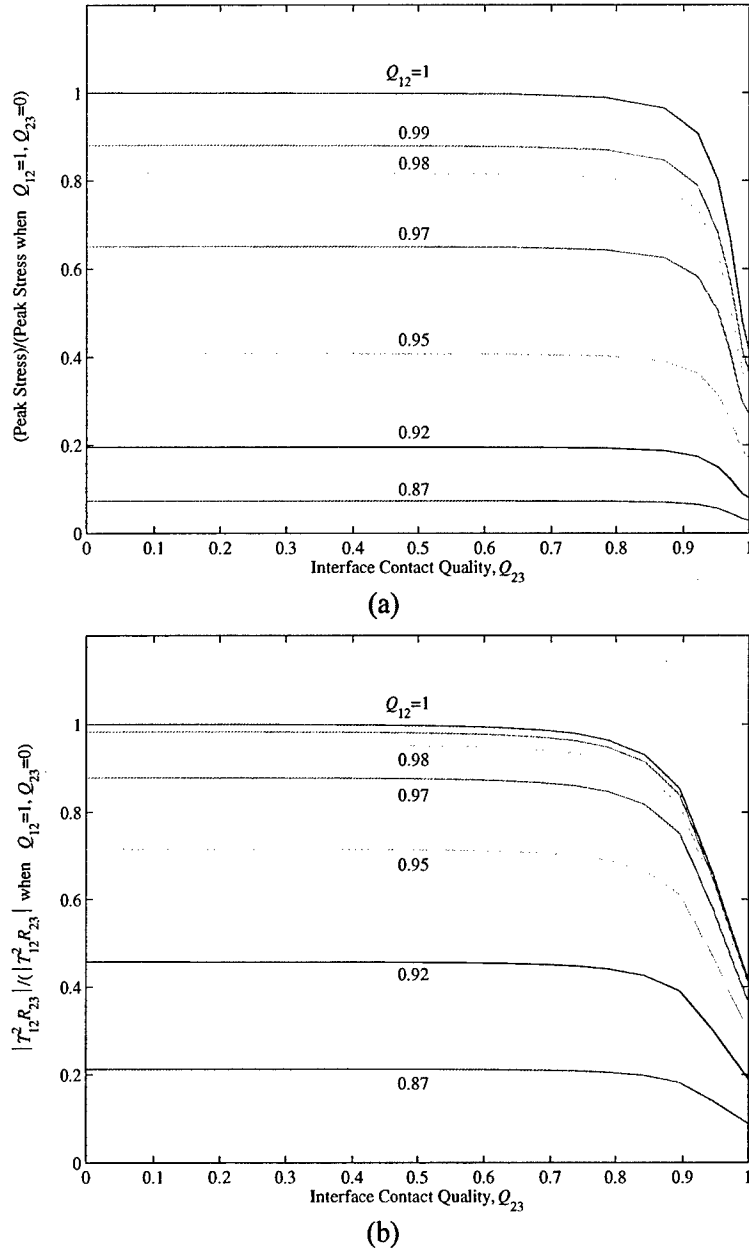
Fig. 17. Normalized magnitudes as Q_{23} varies of (a) peak surface stress in first reflection from second interface in three-layer model and (b) theoretical value of $T_{12}{}^2 R_{23}$.

39
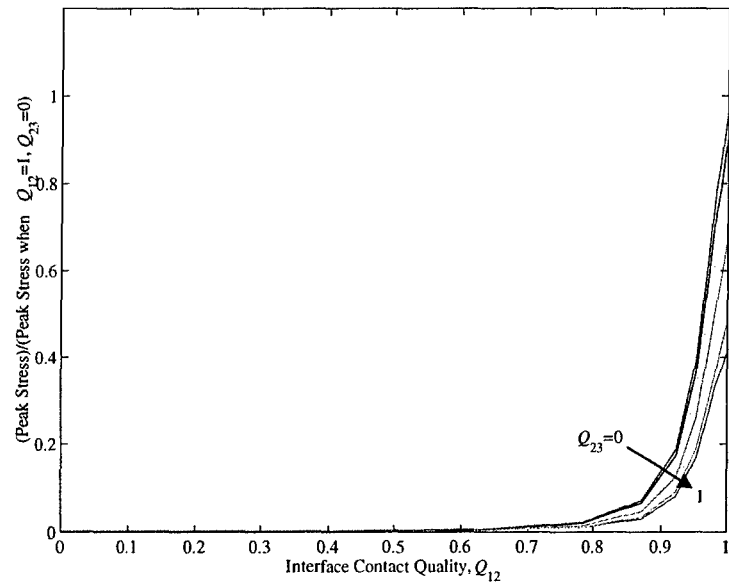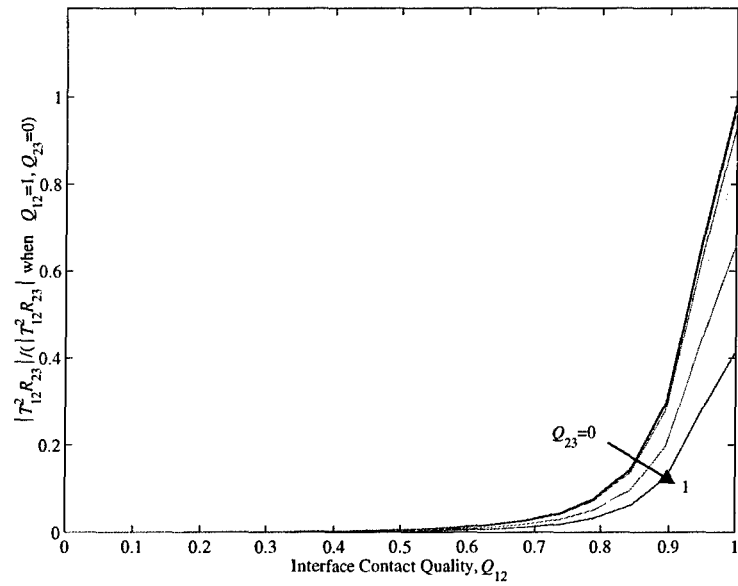
Fig. 18. Normalized magnitudes as Q_{12} varies of (a) peak surface stress in first reflection from second interface in three-layer model and (b) theoretical value of $T_{12}^2 R_{23}$.

In both figures above, the trends between the simulated and theoretical results match closely. There is considerable disagreement between the actual magnitudes in certain cases,

however. The theoretical results are for a single, discrete frequency equal to the center

frequency used in the three-layer model simulation. This model uses a Gaussian-modulated

input signal with a continuous frequency spectrum. As the bandwidth (and frequency content of

the input signal) increases, the actual reflection and transmission coefficients increasingly differ

from the theoretical results obtained with a single frequency. In addition, this difference between

the simulated and theoretical results is essentially cubed as the signal interacts with three

interfaces in the trip from the surface to the second interface and back again. Similar results can

be seen in phase angle of the peak surface stress from the simulation and theoretical phase angle

of $T_{12}{}^2 R_{23}$.

These results can be used to generate a test procedure for and assist in interpreting the

results of ultrasonic NDE of layered composites. Since all reflections from the first interface are

compared to the $Q_{12}{=}0$ (or free surface) case, similar comparisons could be made in an actual

setting to the results seen from a calibration block of equal composition and thickness as the first

layer in the tested laminate. Because of the steepness of the reflection coefficient curves, plots

such as Fig. 15 can be used to select a threshold reflection coefficient to indicate a degraded

bond. For the materials and configuration in this example, a measured reflection coefficient

from the first interface greater than 0.9 indicates a bond quality of approximately 90% or less. A

similar result might be used to select a threshold value for acceptance of a manufactured part.

Analysis of the signals from a second interface is more difficult, but the discussion of

input signal shape from the previous section can assist in obtaining an undistorted reflection and

the plots of Fig. 17 and Fig. 18 can assist in interpreting the results. Test results from a second

calibration block carefully manufactured to represent the first two layers and knowledge of the

first interface bond quality could be used to select a threshold value for acceptance of a second

interface. While it is difficult to more quantitatively assess the bond quality of the interface, a procedure incorporating these concepts could be used to develop accept/reject criteria in ultrasonic NDE procedures.

Recommendations

Understanding of the ultrasonic wave propagation in the proposed structure would benefit from expansion of the three-layer model to two dimensions. A two-dimensional MSDLM exists, and could be easily implemented in order to more accurately model the effects of an ultrasonic transducer (point source) and to better represent flaws of finite dimension. Further study would allow modeling of the reentrant corner of the stiffener in order to improve pulse-echo ultrasonic NDE efforts of this region.

Conclusions

The ultrasonic phase velocity is essentially constant for all three materials in the range of 1.0 to 5.0 MHz. At lower frequencies, interaction between the wavelength and the thickness of the sample may affect the accuracy of the measurement. The global averages of all ultrasonic phase velocity measurements for axis 1 in the FRP, syntactic foam, and resin putty are 2750, 2309, and 2290 m/s respectively. These measured velocities differ from the theoretical values for an unbounded, elastic, isotropic solid by 1, 12, and 25 percent. The attenuation of the three materials is constant or slightly increasing in the range of 1.0 to 3.0 MHz. The global average values of attenuation in axis 1 of the FRP, syntactic foam, and resin putty are 68.2, 33.6, and 58.7 Np/m respectively. The phase velocity and attenuation measurements show the FRP to be approximately transversely isotropic and the resin putty and syntactic foam to be isotropic materials.

The results of simulation of pulse-echo ultrasonic NDE in the three-layer model are useful in understanding the factors involved in obtaining and interpreting ultrasonic signals in thick, layered composites. In layered media with two or more interfaces, overlapping reflections can obscure the signals of interest. Depending on the thickness and phase velocity of each layer, the bandwidth and frequency of the input signal can be adjusted to separate reflections seen at the surface. A minimum required bandwidth to separate the first reflection from the second interface and the second reflection from the first interface is derived. For the case with f_c=2.0

MHz, c_1=2750 m/s, l_1=0.0127 m, $\dfrac{l_2/l_1}{c_2/c_1} = 1.2$, a bandwidth of $\dfrac{f_\sigma}{f_c} \geq 0.25$ is required.

The magnitudes and phase angles of the effective reflection coefficient of the first interface from the three-layer simulation agree closely with the predicted theoretical results. The magnitude of the reflection coefficient remains near one as the interface contact quality Q_{12} increases from zero. Above Q_{12}=0.8, the reflection coefficient drops steeply. As an indication of bond quality in the first interface of layered media, any reflection coefficient above a threshold level is a clear indication of a degraded bond. For the materials and configuration in this example, a measured reflection coefficient from the first interface greater than 0.9 indicates a bond quality of approximately 90% or less. The reflection signals from the second interface in the three-layer model show the same trends as theoretical results. The magnitudes of the reflections from the simulation differ from the theoretical magnitudes because the three-layer model uses an input signal with a continuous frequency spectrum while the theoretical results are based on a single discrete frequency. The three-layer model accurately simulates the behavior of layered viscoelastic solids and is useful in predicting the behavior of the FRP, syntactic foam, and resin putty materials in actual pulse-echo ultrasonic NDE.

43

Page Intentionally Left Blank

Acknowledgements

I would like to thank Professor James H. Williams, Jr. for his excellent guidance and for the superior example he presents. I would also like to thank Anton F. Thomas for many hours of technical support and for his friendship throughout the project. Bruce Bandos and Richard Grassia from the Naval Surface Warfare Center, Carderock Division spent many hours collecting and compiling the material data included within. Thank you to Harry K. Telegadas, also of the Naval Surface Warfare Center, Carderock Division, for the opportunity to work on an interesting and meaningful project. Finally, I must thank my beautiful wife Stacy and our beautiful daughter Clara for their unwavering love and support and endless supply of smiles.

Page Intentionally Left Blank

References

1. Potter, P. *The AMPTIAC Quarterly*. 7:37 (2003).

2. Nguyen, L. *Office of Naval Research US-Pacific Rim Workshop*. Honolulu. (1998).

3. Crane, R.M., J.W. Gillespie, Jr., D. Heider, S. Yarlagadda, and S.G. Advani. *The AMPTIAC Quarterly*. 7:41 (2003).

4. Nguyen, L., J. Beach, and E. Greene. *International Maritime Defence Exhibition*. Singapore. (1999).

5. Bar-Cohen, Y. *Mater. Eval.* 58:17 (2000).

6. Bar-Cohen, Y. *Mater. Eval.* 58:141 (2000).

7. Lipetsky, K.G., and B.G. Bandos. *SAMPE J.* 39:66 (2003).

8. Liu, J.M. *Proc. SPIE Int. Soc. Opt. Eng.* 3396:135 (1998).

9. Green, R.E. *Proc. SPIE Int. Soc. Opt. Eng.* 2459:30 (1995).

10. Dokun, O.D., L.J. Jacobs, and R.M. Haj-Ali. *J. Eng. Mech.* 126:704 (2000).

11. Jones, T.S., and E.A. Lindgren. *Proc. SPIE Int. Soc. Opt. Eng.* 2245:173 (1994).

12. Jones, T.S. *Proc. SPIE Int. Soc. Opt. Eng.* 2459:42 (1995).

13. Mouritz, A.P., C. Townsend, and M.Z. Shah Khan. *Compos. Sci.Technol.* 60:23 (2000).

14. Lu, X., K. Yul Kim, and W. Sachse. *Compos. Sci.Technol.* 57:753 (1997).

15. Balasubramaniam, K., and S.C. Whitney. *NDT E Int.* 29:225 (1996).

16. Frankle, R.S. and D.N. Rose. *Proc. SPIE Int. Soc. Opt. Eng.* 2459:51 (1995).

17. Delsanto, P.P., and M. Scalderandi. *J. Acoust. Soc. Am.* 104:2584 (1998).

18. Christensen, R.M. *Theory of Viscoelasticity: An Introduction* 2nd ed., p. 3-32. Academic Press, New York (1982).

19. Thomas, A.F., H. Yim and J.H. Williams, Jr. Draft (2005).

20. Yim, H. and Y. Sohn. *IEEE Trans. Ultrason. Ferroelectr. Freq. Cont.* 47:549 (2000).

21. Yim, H. and Y. Choi. *Mater. Eval.* 58:889 (2000).

22. Baik, J.M., and R.B. Thompson. *J. Nondestr. Eval.* 4:177 (1984).

23. Graff, K.F. *Wave Motion in Elastic Solids,* p. 84. Dover Publications, New York (1975).

24. Caiazzo, A. Private Communication. Materials Sciences Corporation. 181 Gibraltar Road, Horsham, PA 19044 (March 2005).

25. Lee, S.H., and J.H. Williams, Jr. *J. Nondestr. Eval.* 1:4 (1980).

26. Kolsky, H. *Stress Waves in Solids* 2nd ed., p. 84. Dover Publications, New York (1963).

27. McClintock, F.A. and A.S. Argon. *Mechanical Behavior of Materials*, p. 33. Addison Wesley, Reading (1966).

Appendix A.   Quality Factor

There are numerous methods of characterizing and quantifying the energy loss mechanisms of solids. Williams, et al. have summarized the relationship between different ultrasonic energy loss factors in [A-1]. Kolsky [A-2] collectively labels these mechanisms "internal friction" and defines a "specific loss" $\Delta W/W$ as the ratio of the energy dissipated by the material in one stress cycle to the peak elastic energy stored during the cycle.

Consider a homogeneous plane stress wave of small amplitude σ propagating in the x direction. After traveling some distance x, the stress amplitude will be

$$\sigma = \sigma_0 \exp(-\alpha x) \tag{A. 1}$$

where σ_0 is the stress amplitude at $x=0$ and α is the attenuation (another measure of internal energy loss in solids). The wave enters a control volume of unit area normal to the direction of propagation and length δx. If the material density is ρ and the velocity of propagation is c, the energy entering the control volume per unit time is then

$$E_{in} = \frac{\sigma_0^2 \exp(-\alpha x)}{2\rho c} \tag{A. 2}$$

The energy leaving per unit time is

$$E_{out} = \frac{\sigma_0^2 \exp[-\alpha(x+\delta x)]}{2\rho c} \tag{A. 3}$$

For a small δx, the energy dissipated per unit time is approximately

$$E_{in} - E_{out} \approx \frac{\sigma_0^2 \alpha \delta x \exp(-\alpha x)}{\rho c} \tag{A. 4}$$

and the energy dissipated in one stress cycle of frequency ω is

49

$$\Delta W = \frac{2\pi}{\omega} \frac{\sigma_0^2 \alpha \delta x \exp(-\alpha x)}{\rho c}$$

(A. 5)

The peak elastic energy stored in the slab during the cycle is [A-2]

$$W = \frac{\sigma_0^2 \delta x \exp(-\alpha x)}{2\rho c^2}$$

(A. 6)

Using the wavenumber $k = \dfrac{\omega}{c}$, Eq. (A.5), and Eq. (A.6), the specific loss can be expressed as

$$\frac{\Delta W}{W} = \frac{2\pi}{k/2\alpha}$$

(A. 7)

The quantity $k/2\alpha$ is called the quality factor and is usually denoted by the symbol Q [A-3]. This simplified derivation is but one of many; Carcione and Cavallini arrive at a similar result for homogeneous waves in low-loss solids using complex velocities and attenuation vectors [A-4]. As seen in Eq. (A.7), the quality factor is inversely proportional to the specific loss and thus is another measure of the energy loss in a solid. It can also be thought of as the number of wavelengths λ, where $\lambda = \dfrac{2\pi}{k}$, required to reduce the stress wave amplitude to $e^{-\pi}$ (roughly 4%) of its original value in a material with attenuation α. Setting

$$\sigma_0 \exp(-Q\lambda\alpha) = \sigma_0 \exp(-\pi)$$

(A. 8)

and solving for Q again yields

$$Q = \frac{k}{2\alpha}$$

(A. 9)

References

A-1. Williams, J.H., Jr., S.S. Lee, and H. Nayeb-Hashemi. NASA Contractor Report 3181 (1979).

A-2. Kolsky, H. *Stress Waves in Solids* 2nd ed., p. 99-129. Dover Publications, New York (1963).

A-3. O'Connell, R.J., and B. Budiansky. *Geophys. Res. Letters*, 5:5 (1978).

A-4. J.M. Carcione and F. Cavallini, *Mech. Mater.* 19:311 (1995).

Page Intentionally Left Blank

Appendix B.   High Frequency Assumption

The viscoelastic behavior of the standard linear solid is implemented in the MSDLM algorithm of Thomas et al. [B-1] as a function of the material attenuation α, the relaxation time τ, and a dispersion parameter r, which is a measure of the extent of dispersion in the standard linear solid and is equal to the squared ratio of the minimum phase speed in the material (at low frequency) to the maximum phase speed in the material (at high frequency) [B-1]. The attenuation is a material property, the relaxation time is obtained from an assumed value of $\omega_c \tau$ and a given center frequency ω_c, and the parameter r is calculated from the dispersion equation relating the three together.

While [B-1] includes full derivations of the dispersion relations for phase speed c (or wavenumber k) and attenuation α for all frequency ranges, this implementation of the MSDLM code assumes the standard linear element is in the high frequency limit, where the non-dimensional frequency $\omega_c \tau \gg 1$. Under this condition, the phase speed and attenuation are constant, and the dispersion relations reduce to

$$\alpha = \frac{1-r}{2\tau c} \tag{B. 1}$$

$$k = \frac{\omega_c}{c} \tag{B. 2}$$

When $r=1$, the material is not attenuating and the standard linear solid behaves elastically. When $r=0$, the minimum phase speed in the material is zero, and the standard linear solid acts as a Maxwell model. Solving Eq. (B.1) for τ when $r=0$ and multiplying the result by ω_c give

$$\omega_c \tau = \frac{\omega_c}{2\alpha c} = \frac{k}{2\alpha} \tag{B. 3}$$

Since $0 \leq r \leq 1$, Eq. (B.3) can be used to find the upper bound for $\omega_c \tau$ for a given ω_c in a material of known α and c. The results above apply to both longitudinal and shear waves if the appropriate phase speed is used.

The lower bound for $\omega_c \tau$ is determined by investigating the errors between the calculated values of phase speed and attenuation at each $\omega_c \tau$ and the theoretical values in the high frequency limit. Using the dispersion relations in [B-1], Fig. B.1 shows the maximum of these two errors as a function of r and $\omega_c \tau$. The maximum error is only weakly dependent on r, and highly dependent on $\omega_c \tau$. The maximum error can be kept below 1% by selecting $\omega_c \tau \geq 5$. As long as

$$\frac{k}{2\alpha} \geq 5 \qquad (B.4)$$

for the material (with attenuation α) and frequency of interest, setting the relaxation time of the standard linear element in the MSDLM to

$$\tau = \frac{5}{\omega_c} \qquad (B.5)$$

will ensure phase speed and attenuation errors from the high frequency assumption will be less than 1%. Setting the relaxation time to the lower bound reduces numerical computation time.

Logarithm of Normalized Frequency, $\log_{10}(\omega\tau)$

Dispersion Coefficient, r

Maximum Logarithmic Error of Attenuation and Phase Speed,

$$\max\left[\left|\log_{10}\frac{\alpha_{max}-\alpha}{\alpha_{max}}\right|, \left|\log_{10}\frac{c_{max}-c}{c_{max}}\right|\right]$$
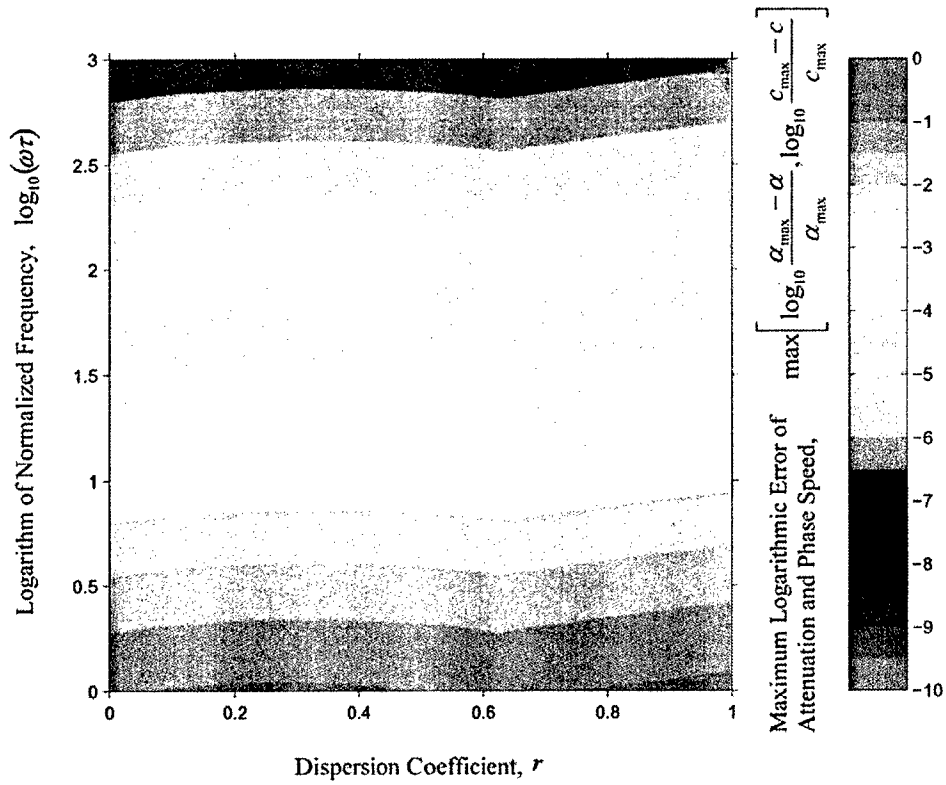
Fig. B. 1. Maximum error of phase speed c and attenuation α relative to high frequency values c_{max} and α_{max}, as a function of dispersion coefficient r and normalized frequency $\omega_c\tau$.

References

B-1. Thomas, A.F., H. Yim and J.H. Williams, Jr. Draft. (2005).

Appendix C.   Imperfect Interface of Dissimilar Materials

Consider the interface of two dissimilar materials at particle N located at $x=0$ as shown in Fig. C.1. In one dimension and in the absence of body forces, the equation of motion of a half-particle k adjacent to an interface can be written as

$$f_k = \frac{\rho_k}{2}\ddot{u}_k \qquad (C.1)$$

where f_k is the net force per unit volume acting on half-particle k, ρ_k is its density, and u_k is its displacement. If the contact force between half-particles at the interface is f_{ct}, the acceleration of each half particle can be written as

$$\ddot{u}_{N^-} = \frac{2}{\rho_I}\left(f_{ct} - f_{N-\frac{1}{2}}\right) \qquad (C.2)$$

$$\ddot{u}_{N^+} = \frac{2}{\rho_{II}}\left(f_{N+\frac{1}{2}} - f_{ct}\right) \qquad (C.3)$$
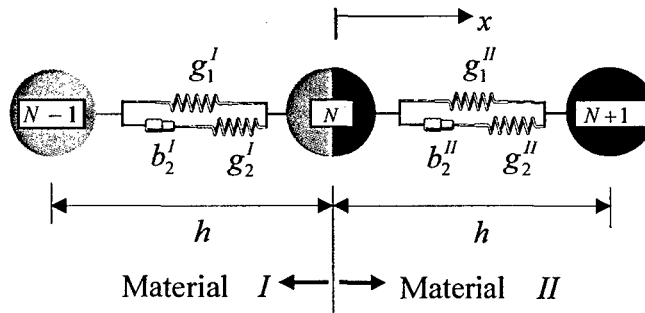
Fig. C. 1. One-dimensional MSDLM model of imperfect interface of dissimilar materials near position N, at $x=0$, where h is grid spacing, and various g and b are respective spring constants and dashpot coeffiecients related to governing PDEs of each standard linear solid [C-1].

57

If perfect contact exists between half-particles at the interface, Eq. (C.2) and Eq. (C.3) can be equated and the contact force can be written as

$$f_{ct} = \frac{\rho_I f_{N+\frac{1}{2}} + \rho_{II} f_{N-\frac{1}{2}}}{\rho_I + \rho_{II}}$$ (C. 4)

The concept of a general imperfect interface is introduced following the method of Delsanto and Scalerandi [C-2]. The bond quality at the interface is represented by a parameter Q called contact quality. Q may vary between $Q=0$ (no bond) and $Q=1$ (perfect bond). The contact force of Eq. (C.4) is re-written as

$$f_{ct} = Q\left(\frac{\rho_I f_{N+\frac{1}{2}} + \rho_{II} f_{N-\frac{1}{2}}}{\rho_I + \rho_{II}}\right)$$ (C. 5)

Subtracting Eq. (C.2) from Eq. (C.3) and inserting Eq. (C.5) gives

$$\ddot{u}_{N^+} - \ddot{u}_{N^-} = 2\left(\frac{\rho_I + \rho_{II}}{\rho_I \rho_{II}}\right)\left(\frac{1-Q}{Q}\right)f_{ct}$$ (C. 6)

Further, following Baik and Thompson [C-3], an interfacial stiffness K per unit area can be defined as

$$K = \frac{\sigma}{u(0^+) - u(0^-)}$$ (C. 7)

where half particle N^+ is at $x=0^+$ and N^- is at $x=0^-$. This can be thought of as the stiffness of a massless spring between adjacent particles at the interface as shown in Fig. C. 2.
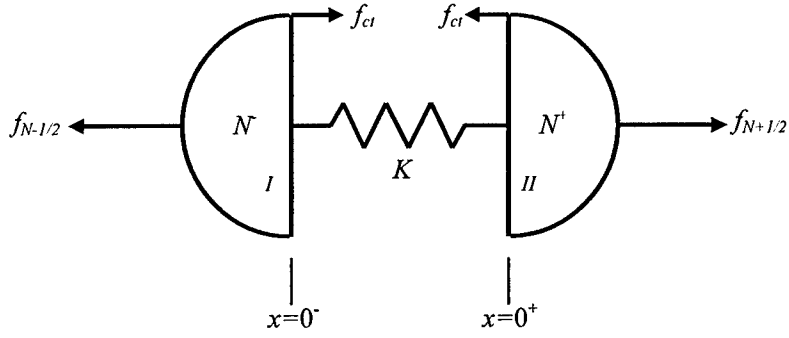
Fig. C. 2. Imperfect interface between materials *I* and *II* at particle *N*, at *x*=0, where *K* is interfacial stiffness, f_{ct} is contact force, and $f_{N-1/2}$ and $f_{N+1/2}$ are forces from adjacent particles in grid.

The stress and displacement boundary conditions can be written as [C-3]

$$\frac{1}{2}\left[\sigma(0^+) + \sigma(0^-)\right] \approx K\left[u(0^+) - u(0^-)\right] \qquad \text{(C. 8)}$$

$$\sigma(0^+) - \sigma(0^-) = 0 \qquad \text{(C. 9)}$$

Remembering that f_{ct} is a force per unit volume, the stress at the interface is

$$\sigma(0^+) = \sigma(0^-) = hf_{ct} \qquad \text{(C. 10)}$$

where *h* is the spacing between particles in the grid. Substituting Eq. (C.10) into Eq. (C.8) gives

$$u(0^+) - u(0^-) = \frac{1}{K}hf_{ct} \qquad \text{(C. 11)}$$

Now consider an incident harmonic longitudinal wave of frequency ω at the interface

$$u_I(x,t) = u_p e^{i(k_1 x - \omega t)} \qquad \text{(C. 12)}$$

a reflected wave

$$u_R(x,t) = Ru_p e^{i(-k_1 x - \omega t)} \qquad \text{(C. 13)}$$

and a transmitted wave

$$u_T(x,t) = Tu_p e^{i(k_2 x - \omega t)} \qquad \text{(C. 14)}$$

where u_p is an arbitrary initial displacement, k is the wavenumber, $i \equiv \sqrt{-1}$, and t is time. R and T are the reflection and transmission coefficients. Using conservation of energy at the interface ($x=0$), the displacement across the interface can be written as

$$u(0^+) - u(0^-) = (T - 1 - R)e^{-i\omega t} \qquad \text{(C. 15)}$$

Similarly,

$$\ddot{u}(0^+) - \ddot{u}(0^-) = -\omega^2 (T - 1 - R)e^{-i\omega t} \qquad \text{(C. 16)}$$

Combining Eqs. (C.11), (C.15), and (C.16), and equating with Eq. (C.6) give

$$K = \frac{h\omega^2}{2} \left(\frac{\rho_I \rho_{II}}{\rho_I + \rho_{II}} \right) \left(\frac{Q}{Q-1} \right) \qquad \text{(C. 17)}$$

The interfacial stiffness K is then a function of the material properties, the frequency, and the interface contact quality Q. As $Q \to 0$, the stiffness $K \to 0$ and there is no connection between particles. As $Q \to 1$, the stiffness K becomes infinite, and a perfect bond is achieved.

The transmission and reflection coefficients can be derived via a similar procedure. The incident, reflected, and transmitted waves of Eqs. (C.12)-(C.14) at an arbitrary time ($t=0$) can be used with Eq. (C.9), Eq. (C.11), and

$$\sigma = \rho c^2 \frac{\delta u}{\delta x} \qquad \text{(C. 18)}$$

and

$$k = \frac{\omega}{c} \qquad \text{(C. 19)}$$

where c is phase speed to solve for T and R

$$T = \frac{\dfrac{2Z_I}{Z_I + Z_{II}}}{1 - \dfrac{i\omega}{K}\dfrac{Z_I Z_{II}}{Z_I + Z_{II}}}$$

(C. 20)

$$R = \frac{\dfrac{Z_I - Z_{II}}{Z_I + Z_{II}} - \dfrac{i\omega}{K}\dfrac{Z_I Z_{II}}{Z_I + Z_{II}}}{1 - \dfrac{i\omega}{K}\dfrac{Z_I Z_{II}}{Z_I + Z_{II}}}$$

(C. 21)

The Z coefficients are the elastic impedances of each material [C-4]

$$Z = \rho c$$

(C. 22)

When $Q \to 1$ and $K \to \infty$, the transmission and reflection coefficients for a perfect boundary are

$$T_{perfect} = \frac{2Z_I}{Z_I + Z_{II}}$$

(C. 23)

$$R_{perfect} = \frac{Z_I - Z_{II}}{Z_I + Z_{II}}$$

(C. 24)

When $Q \to 0$ and $K \to 0$, the results for a free surface are

$$T_{freesurface} = 0$$

(C. 25)

$$R_{freesurface} = 1$$

(C. 26)

Figure C. 3 shows the magnitudes of the reflection and transmission coefficients for two identical (equal impedance) half-spaces across an interface of varying contact quality.
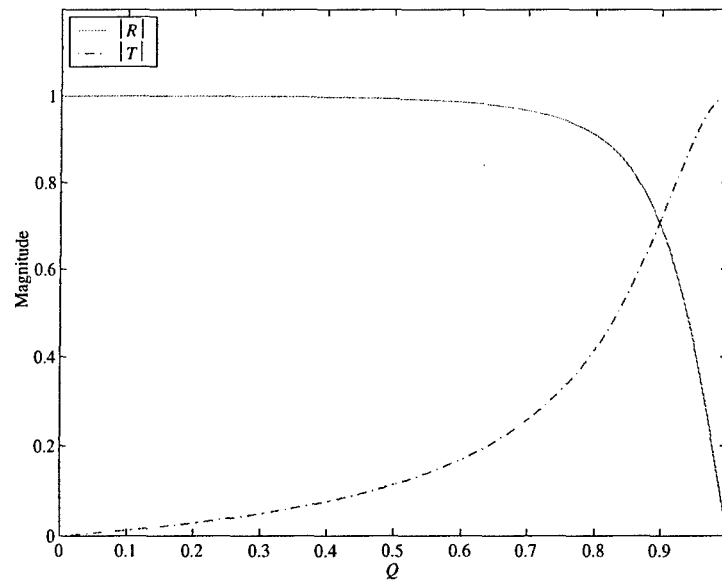
Fig. C. 3. Magnitudes of reflection and transmission coefficients, R and T, of two identical half spaces with $c=2750$m/s, $\rho=1882$ kg/m^3, $f=2.0$ MHz, $h=0.0001$ m as a function of interface contact quality Q.

References

C-1. Thomas, A.F., H. Yim and J.H. Williams, Jr. Draft. (2005).

C-2. Delsanto, P.P., and M. Scalderandi. *J. Acoust. Soc. Am.* 104:2584 (1998).

C-3. Baik, J.M., and R.B. Thompson. *J. Nondestr. Eval.* 4:177 (1984).

C-4. Graff, K.F. *Wave Motion in Elastic Solids,* p. 84. Dover Publications, New York (1975).

Page Intentionally Left Blank

Appendix D.   Material Data Analysis

Ultrasonic phase velocity and amplitude measurements were taken from the test

specimens in Table D. 1 over a range of frequencies from 0.1 to 5.0 MHz.

Table D. 1. Test specimen summary.

Material	Number of Cubes	Nominal Dimension
FRP	2	1.42 cm
FRP	2	5.08 cm
Syntactic Foam	1	2.54 cm
Syntactic Foam	1	5.08 cm
Syntactic Foam	1	7.62 cm
Resin Putty	1	2.54 cm
Resin Putty	1	5.08 cm
Resin Putty	1	7.62 cm

The cubic samples enable velocity measurements and attenuation calculations in three

orthogonal directions. Each axis of each cube is labeled as 1, 2, or 3. Figure D. 1 shows the

orientation of the coordinate axes for the FRP laminate. The 1 direction is perpendicular to the

plane of the plies, and represents the direction of interest for the one-dimensional, through-

thickness NDE represented by the MSDLM model. The actual FRP cubes can be seen in

Fig. D. 2.
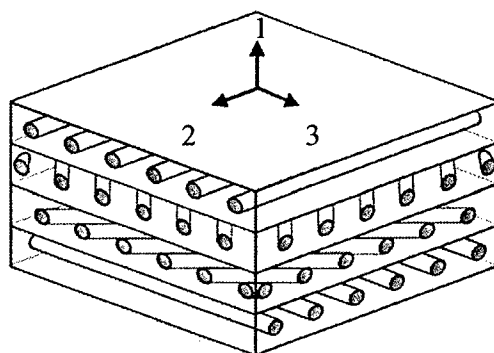
Fig. D. 1. Coordinate axes for FRP test specimens.
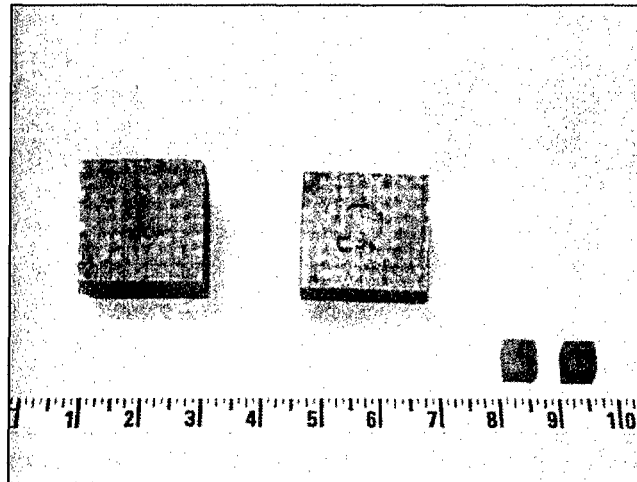
Fig. D. 2. FRP material specimens. Units are in.

The measurements for axis 1 of the FRP material are seen in Fig. D. 3. The measured

phase velocities of the larger samples are consistently greater than those of the smaller samples

for any given frequency. This trend is seen consistently in all three materials, and is a result of

the calibration procedure of the ultrasonic flaw detector used to take the phase velocity

measurements.

Fig. D. 3. FRP axis 1 measured ultrasonic phase velocity. Two cubes of two sizes were measured at each frequency. Data taken with PANAMETRICS-NDT™ EPOCH 4 flaw detector in through-transmission mode at 31.1 dB gain and K B-Aerotech, type Alpha, 5 MHz, 1.27cm diameter, hard-faced transducers with water couplant.

Since the average difference between measurements of differently-sized samples at a given frequency is on the order of five percent, the phase velocity measurements of the differently sized samples at each frequency are simply averaged together. Further, since the phase velocity measurements show little variation with frequency, a global average of all the data points within an axis and frequency is calculated. These results for FRP axis 1 are shown in Fig. D. 4. In all plots, the height of the error bar at each data point is equal to one standard deviation s as calculated by

$$s = \sqrt{\frac{n\sum x_i - \left(\sum x_i\right)^2}{n^2}}$$

(D. 1)

where n is the number of samples and x_i are the individual measurements $i=1,2,\ldots,n$.

Fig. D. 4. FRP axis 1 ultrasonic phase velocity. Points on the solid line represent the mean of four data points at that frequency. The height of the error bar represents one standard deviation for those four points. The dotted line and its error bars are the average and standard deviation of all data points.

Two outlier data points can be seen in Fig. D. 3 at 1 MHz and 5.05 cm and 2 MHz and 1.42 cm. These points are not included in either the average value of phase velocity within a frequency or the global average calculation. In order to prevent artificially skewing the average value within a frequency where an outlier of one size was discarded, a corresponding data point of the other dimension at this frequency is also omitted. The complete data are included in [Appendix F].

As a basis of comparison for the global average value of ultrasonic phase velocity in each material, the theoretical phase velocity of a longitudinal wave in an infinite, elastic, isotropic material is calculated using [D-1]

$$c_{theoretical} = \sqrt{\frac{\lambda + 2\mu}{\rho}}$$

(D. 2)

where c is phase velocity, ρ is density, and λ and μ are the first and second Lamé constants.

These are calculated by [D-2]

$$\lambda = \frac{Ev}{(1+v)(1-2v)} \qquad (D.3)$$

$$\mu = \frac{E}{2(1+v)} \qquad (D.4)$$

where E is the modulus of elasticity and v is Poisson's ratio. The theoretical phase velocities are calculated using values of E, v, and ρ provided with the material samples. These representative elastic material data do not represent actual values of the specific lots of material from which the samples were gathered. Table D. 2 shows both the theoretical and global average velocities for each material. The global averages are within 12% of the calculated theoretical values for all three axes of the FRP and the syntactic foam, but the global average of the resin putty phase velocity is significantly higher than the theoretical value. In addition to the fact that the theoretical results assume elastic and isotropic materials, slight variations in batches of foam and resin putty may cause the elastic properties of the actual samples to differ from the representative values provided.

Table D. 2 Theoretical and measured average phase velocity. Values of E, ρ, and v were provided with material samples. λ, μ, and $c_{theoretical}$ are calculated assuming elastic materials.

	FRP Axis 1	FRP Axis 2	FRP Axis 3	Syntactic Foam	Resin Putty
Density ρ (kg/m³)	1882	1882	1882	512	1245
Modulus of Elasticity E (GPa)	10.4	24.1	24.1	2.2	3.1
Poisson's Ratio v	0.314	0.135	0.099	0.350	0.300
First Lamé Constant λ (GPa)	6.7	3.9	2.7	1.9	1.8
Second Lamé Constant μ (GPa)	4.0	10.6	11.0	0.8	1.2
Theoretical Phase Velocity $c_{theoretical}$ (m/s)	2785	3656	3618	2626	1831
Global Average Measured Phase Velocity (m/s)	2750	3406	3341	2309	2290
% Difference	1%	7%	8%	12%	-25%

The measured ultrasonic phase velocities and calculated averages for the FRP samples in
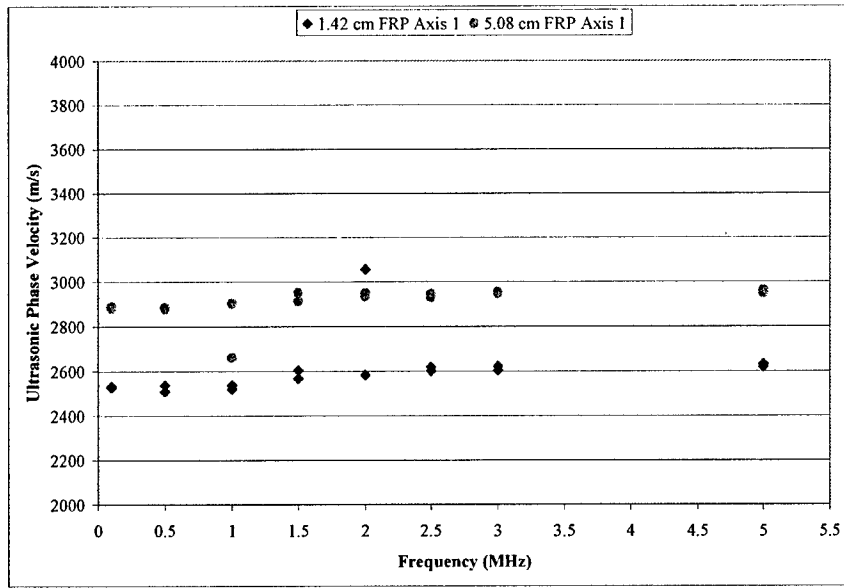
axes 2 and 3 can be seen in Figs. D. 5 through D. 8.
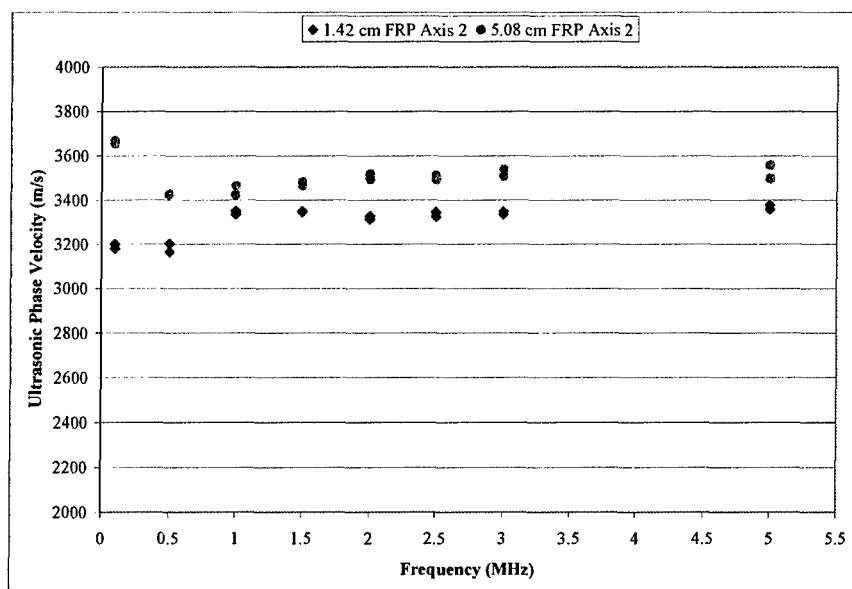
Fig. D. 5. FRP axis 2 ultrasonic phase velocity. Two cubes of two sizes were measured at each frequency. Data taken with PANAMETRICS-NDT™ EPOCH 4 flaw detector in through-transmission mode at 31.1 dB gain and K B-Aerotech, type Alpha, 5 MHz, 1.27 cm diameter, hard-faced transducers with water couplant.
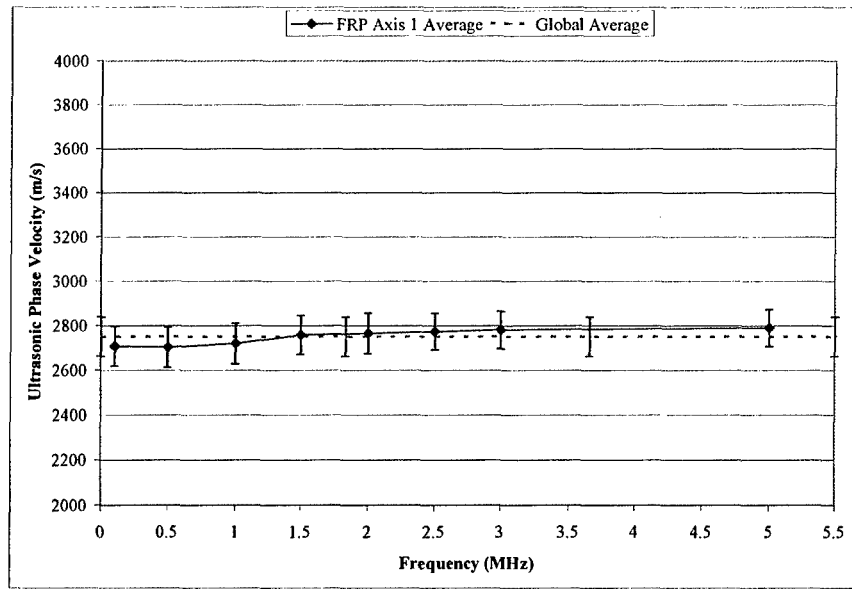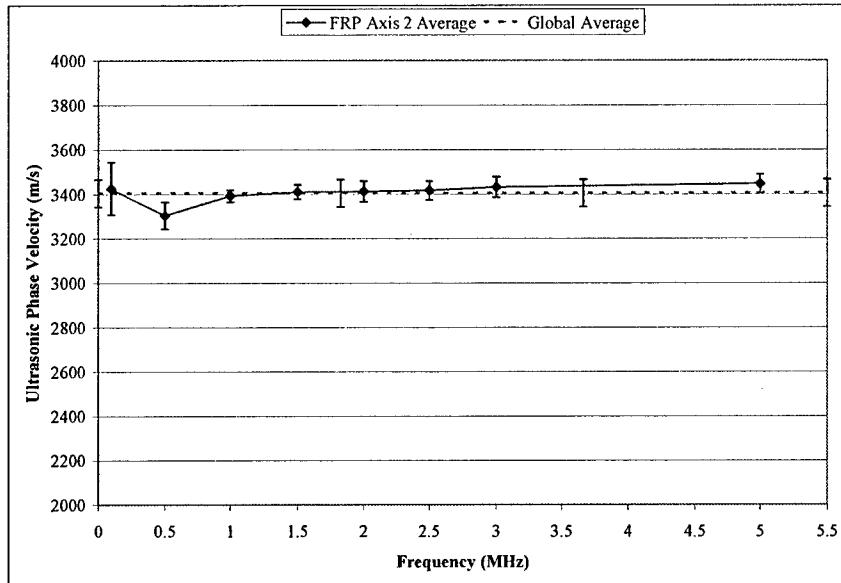
Fig. D. 6. FRP axis 2 ultrasonic phase velocity. Points on the solid line represent the mean of four data points at that frequency. The height of the error bar represents one standard deviation for those four points. The dotted line and its error bars are the average and standard deviation of all data points.
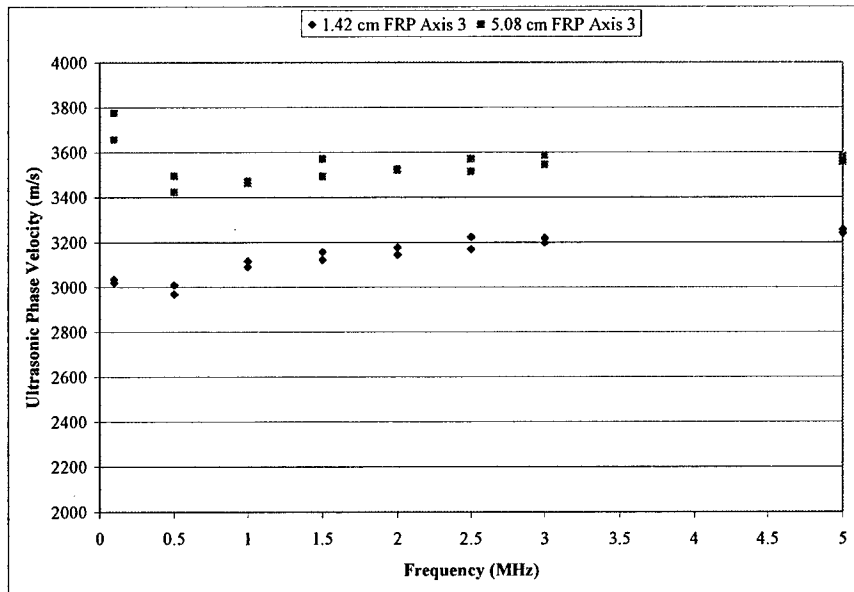
Fig. D. 7. FRP axis 3 ultrasonic phase velocity. Two cubes of two sizes were measured at each frequency. Data taken with PANAMETRICS-NDT[TM] EPOCH 4 flaw detector in through-transmission mode at 31.1 dB gain and K B-Aerotech, type Alpha, 5 MHz, 1.27 cm diameter, hard-faced transducers with water couplant.

71
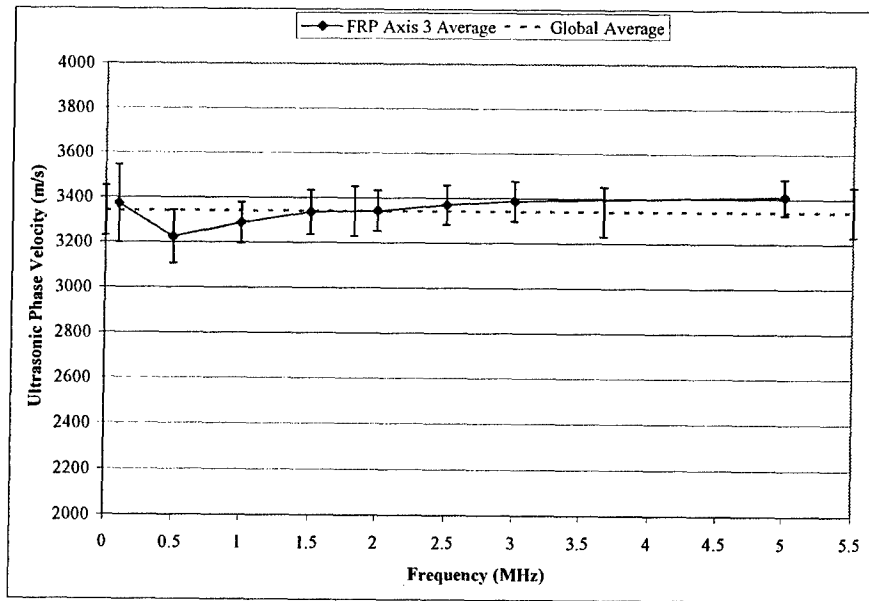
Fig. D. 8. FRP axis 3 ultrasonic phase velocity. Points on the solid line represent the mean of four data points at that frequency. The height of the error bar represents one standard deviation for those four points. The dotted line and its error bars are the average and standard deviation of all data points.

The FRP material is expected to behave in a somewhat transversely isotropic manner. As expected, the average phase velocities in axes 2 and 3 (the plane of the fiberglass cloth) are very similar and greater than the velocity in axis 1 (through the plies). In addition, Figs. D. 4, D. 6, and D. 8 show that the ultrasonic phase velocity in the FRP material is relatively constant with increasing frequency.

An unexpected dip in ultrasonic phase velocity is seen at low frequency in FRP axes 2 and 3. This unexplained behavior was seen sporadically in all three materials throughout multiple data collection events with different transducers. One possible source of this behavior is interaction between the wavelength of the ultrasonic signal at low frequency and the thickness of the sample. At 0.1 MHz in a 2.54 cm sample, the ratio $\frac{l}{\lambda}$ is on the order of 1.0 for these materials, where l is the sample thickness and λ is the wavelength. The trend is not seen

consistently, however. For example, as can be seen in Figs. D.5 and D.7, the dip in velocity in FRP axes 2 and 3 is much more prominent in the 5.08 cm samples than in the 1.42 cm samples. Another possible source of spurious variation is transducer resonance. Regardless of the source of this dip at low frequencies, the ultrasonic phase speed of the FRP material is considered constant above 1.0 MHz.

The attenuation $\alpha(\omega)$ is calculated using the ultrasonic through-transmission output signal amplitudes (A_1, A_2) of two otherwise identical specimens of differing thicknesses (l_1, l_2; $l_2 > l_1$) at a given input frequency ω [D-1].

$$\alpha(\omega) = \frac{\ln(A_1/A_2)}{l_2 - l_1} \qquad (D.\ 5)$$

With two blocks each of two different thicknesses of FRP samples, there are four possible attenuation calculations at any one frequency. The calculated values of attenuation for FRP axis 1 are shown in Fig. D. 9. The attenuation is generally expected to increase with increasing frequency. For all three axes of the FRP material, the data points at 5.0 MHz show a significant decrease in attenuation. The relative difficulty of obtaining the ultrasonic through-transmission amplitudes as such high frequencies make these data somewhat questionable. For this reason all the data points for the FRP material at 5.0 MHz are not considered in any average value calculations. Further, odd trends are seen in the attenuation measurements in all three materials below 1.0 MHz and these data are not included in any average value calculations either.

73
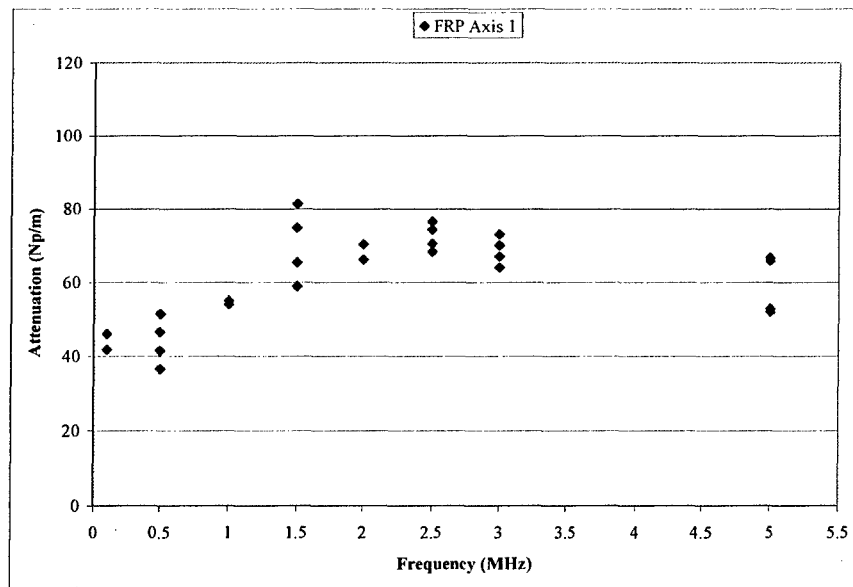
Fig. D. 9. FRP axis 1 attenuation. Two cubes each of two sizes allow for four attenuation calculations at each frequency. Data taken with PANAMETRICS-NDT™ EPOCH 4 flaw detector in through-transmission mode at 31.1 dB gain and K B-Aerotech, type Alpha, 5 MHz, 1.27cm diameter, hard-faced transducers with water couplant.

Similar to the procedure used with the FRP ultrasonic phase velocity, all four data points within a frequency are averaged together. Despite the fact that the attenuation displays much more variation with frequency, a global average value of attenuation is calculated for use in the three layer model (which assumes constant attenuation). These averaged results for FRP axis 1 are seen in Fig. D. 10.
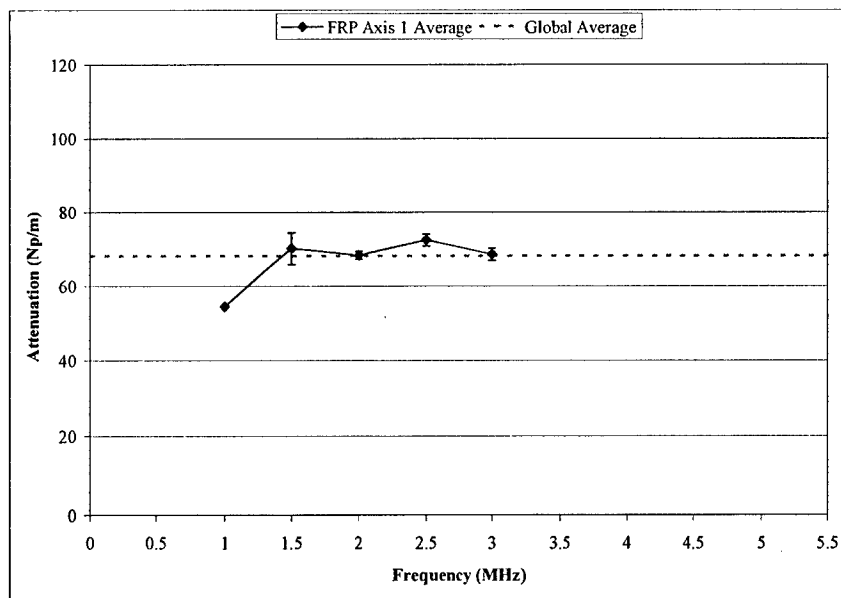
Fig. D. 10. FRP axis 1 attenuation average values. Points on the solid line represent the mean of four data points at that frequency. The height of the error bar represents one standard deviation for those four points. The dotted line and its error bars are the average and standard deviation of all data points in frequency range shown.

The attenuation data points and average values for FRP axes 2 and 3 are seen in Figs. D. 11 through D. 14.

Fig. D. 11. FRP axis 2 attenuation. Two cubes each of two sizes allow for four attenuation calculations at each frequency. Data taken with PANAMETRICS-NDT™ EPOCH 4 flaw detector in through-transmission mode at 31.1 dB gain and K B-Aerotech, type Alpha, 5 MHz, 1.27 cm diameter, hard-faced transducers with water couplant.

Fig. D. 12. FRP axis 2 attenuation average values. Points on the solid line represent the mean of four data points at that frequency. The height of the error bar represents one standard deviation for those four points. The dotted line and its error bars are the average and standard deviation of all data points in frequency range shown.

Fig. D. 13. FRP axis 3 attenuation. Two cubes each of two sizes allow for four attenuation calculations at each frequency. Data taken with PANAMETRICS-NDT™ EPOCH 4 flaw detector in through-transmission mode at 31.1 dB gain and K B-Aerotech, type Alpha, 5 MHz, 1.27 cm diameter, hard-faced transducers with water couplant.

Fig. D. 14. FRP axis 3 attenuation average values. Points on the solid line represent the mean of four data points at that frequency. The height of the error bar represents one standard deviation for those four points. The dotted line and its error bars are the average and standard deviation of all data points in frequency range shown.

Ultrasonic phase velocity and through-transmission amplitude measurements were taken at the same frequencies for syntactic foam and resin putty samples from Table D. 1. The actual specimens are seen in Figs. D. 15 and D. 16.
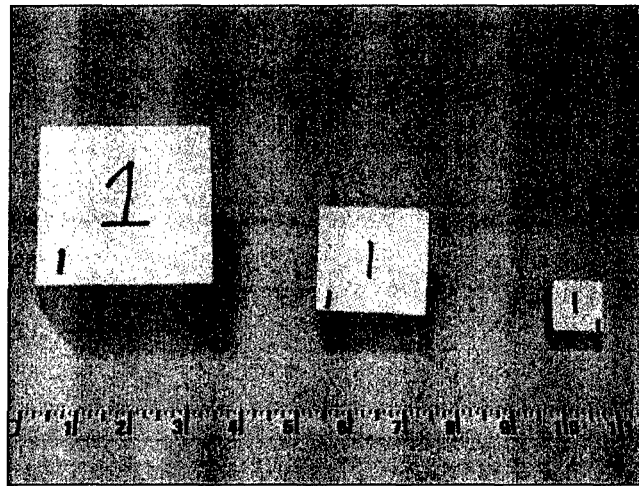
Fig. D. 15. Syntactic foam material specimens. Units are in.
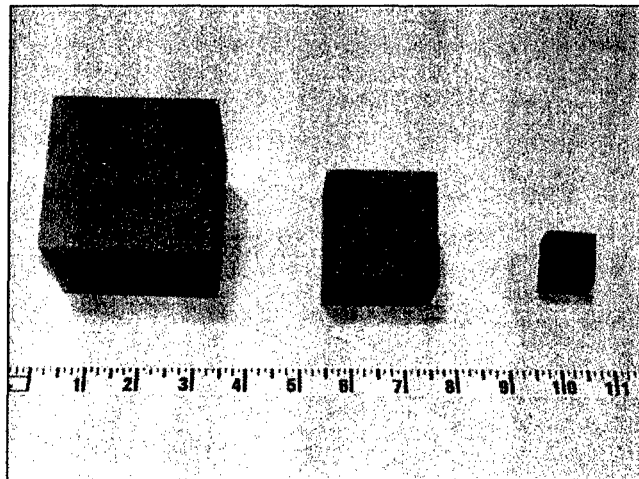
Fig. D. 16. Resin putty material specimens. Units are in.

Preliminary testing showed the foam and resin materials to be isotropic in phase velocity and attenuation. For the final data acquisition, measurements were only taken from one axis.

78

Average values within a frequency and a global average phase velocity are calculated as with the FRP. Figures D. 17 through D. 20 show the actual velocity measurements and averaged values for the foam and resin putty materials. Again the larger specimens display larger ultrasonic phase velocities. Despite their differing constitutions, the syntactic foam and resin putty have nearly identical ultrasonic phase velocities, regardless of frequency or sample thickness.
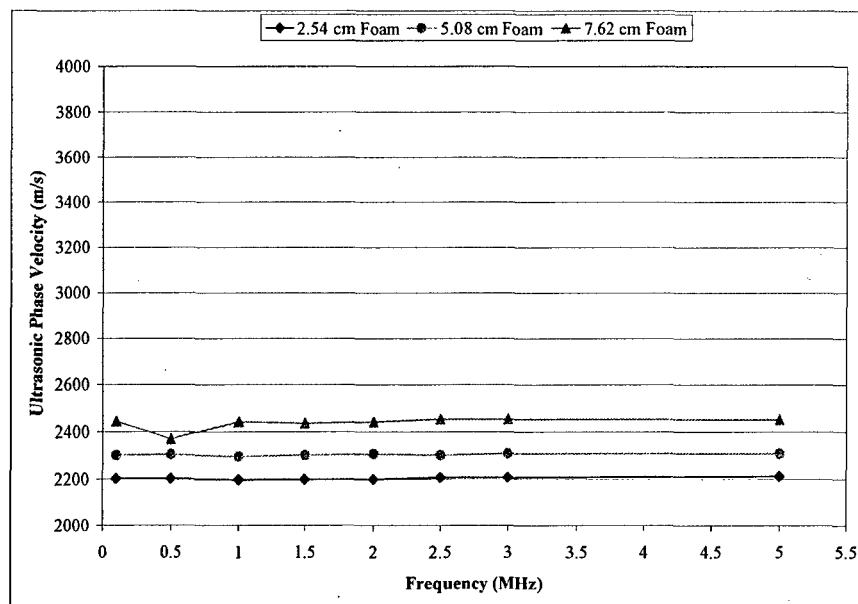
Fig. D. 17. Syntactic Foam axis 1 ultrasonic phase velocity. Data taken with PANAMETRICS-NDT™ EPOCH 4 flaw detector in through-transmission mode at 31.1 dB gain and K B-Aerotech, type Alpha, 5 MHz, 1.27 cm diameter, hard-faced transducers with water couplant.
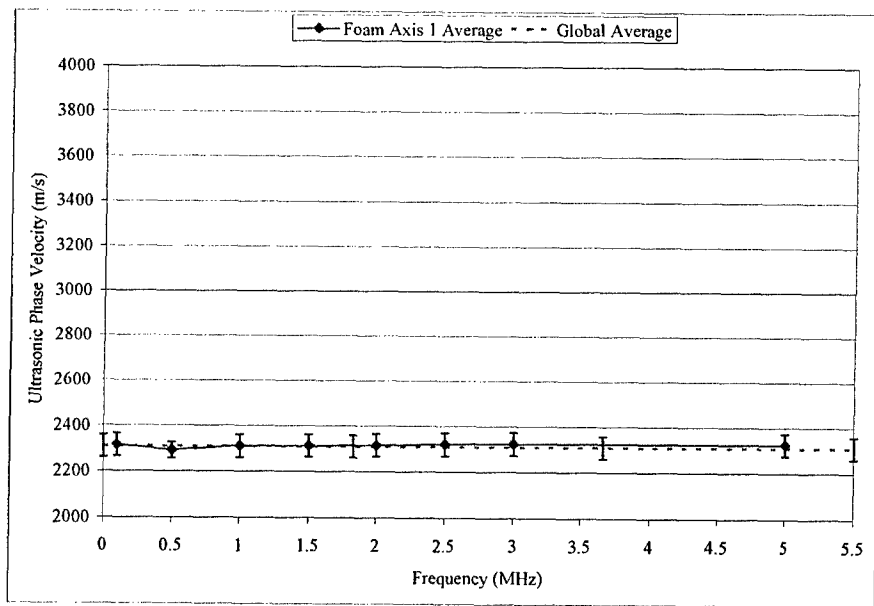
Fig. D. 18. Syntactic foam axis 1 averaged ultrasonic phase velocity. Points on the solid line represent the mean of three data points at that frequency. The height of error bar represents one standard deviation for those three points. The dotted line and its error bars are the average and standard deviation of all data points.
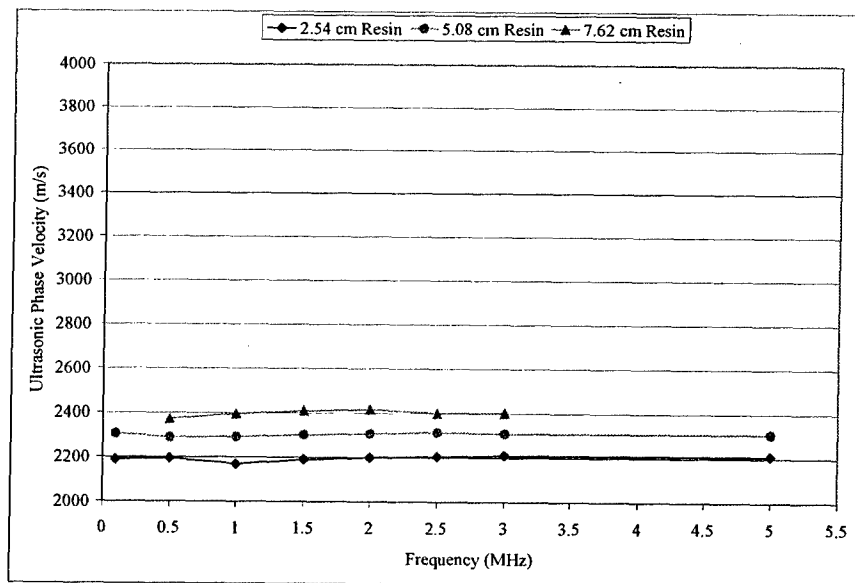
Fig. D. 19. Resin putty axis 1 ultrasonic phase velocity. Data taken with PANAMETRICS-NDT™ EPOCH 4 flaw detector in through-transmission mode at 31.1 dB gain and K B-Aerotech, type Alpha, 5 MHz, 1.27 cm diameter, hard-faced transducers with water couplant.
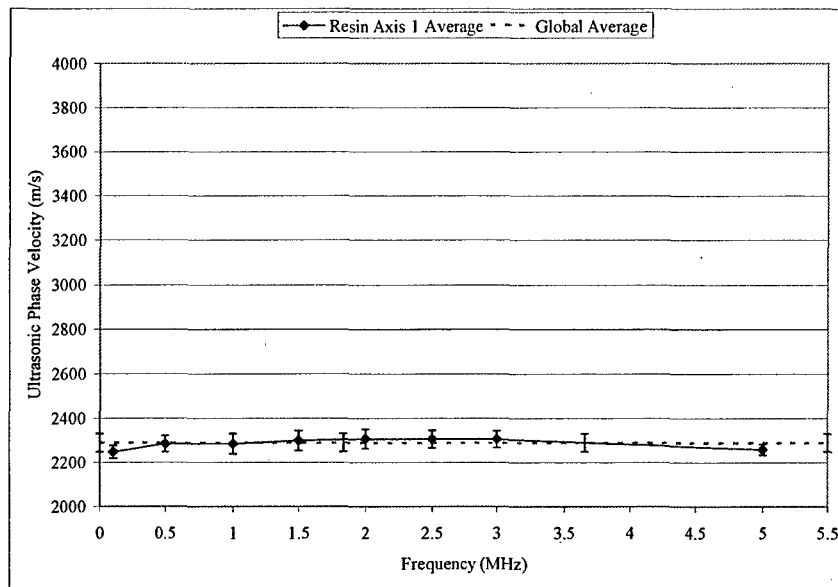
Fig. D. 20. Resin putty axis 1 averaged ultrasonic phase velocity. Points on the solid line represent the mean of three data points at that frequency. The height of error bar represents one standard deviation for those three points. The dotted line and its error bars are the average and standard deviation of all data points.

Three differently-sized blocks of syntactic foam and resin putty enable three different attenuation calculations at each frequency. The results of the attenuation calculations and average values can be seen in Figs. D. 22 through D. 25. Again some unexpected variability is seen in the data below 1.0 MHz and these data are not used in any average value calculations. In general, the attenuation for all three materials is slightly increasing in the range of 1.0 to 3.0 MHz.
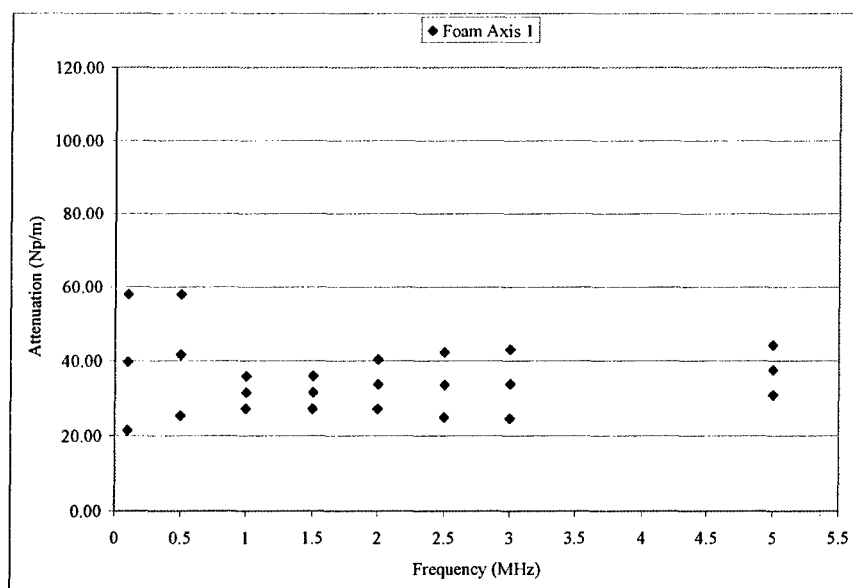
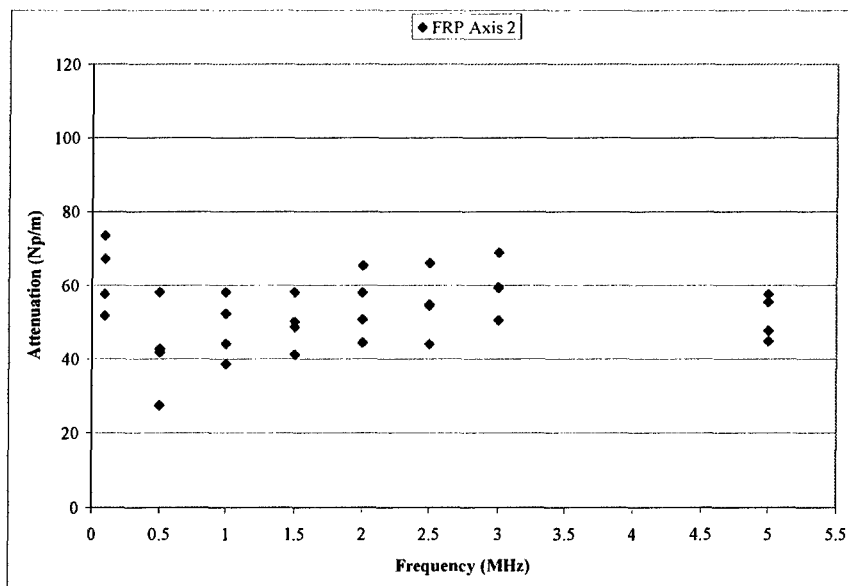**Fig. D. 21.** Syntactic foam axis 1 attenuation. One cube each of three sizes allow for three attenuation calculations at each frequency. Data taken with PANAMETRICS-NDT™ EPOCH 4 flaw detector in through-transmission mode at 31.1 dB gain and K B-Aerotech, type Alpha, 5 MHz, 1.27 cm diameter, hard-faced transducers with water couplant.
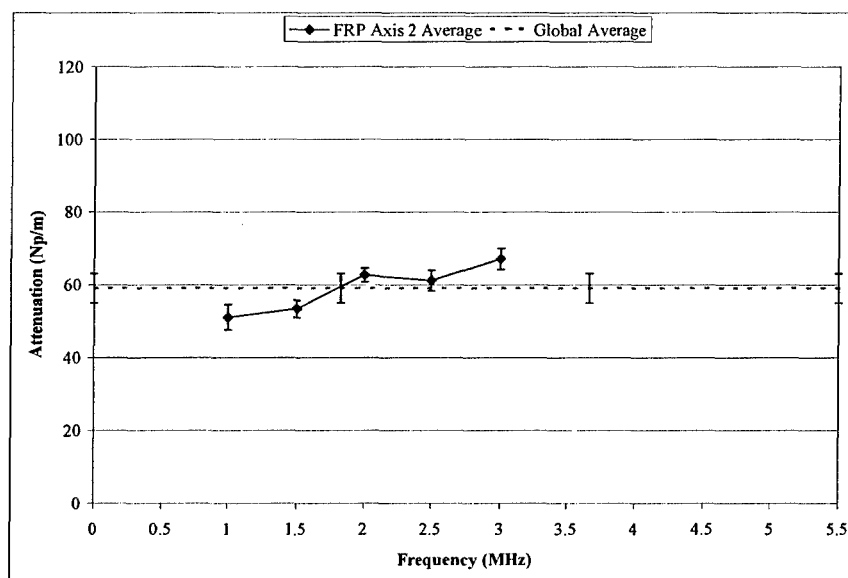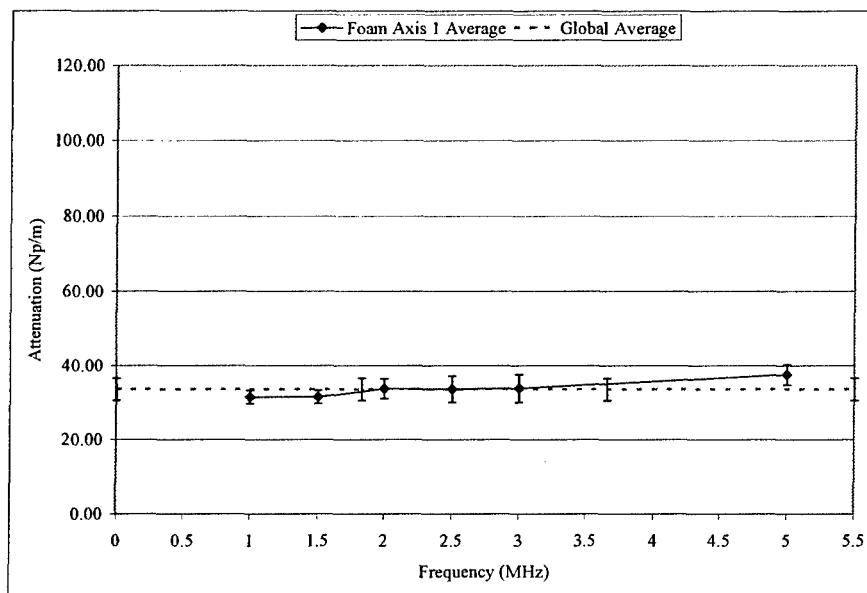

Fig. D. 22. Syntactic foam axis 1 attenuation average values. Points on the solid line represent the mean of three data points at that frequency. The height of the error bar represents one standard deviation for those three points. The dotted line and its error bars are the average and standard deviation of all data points in frequency range shown.
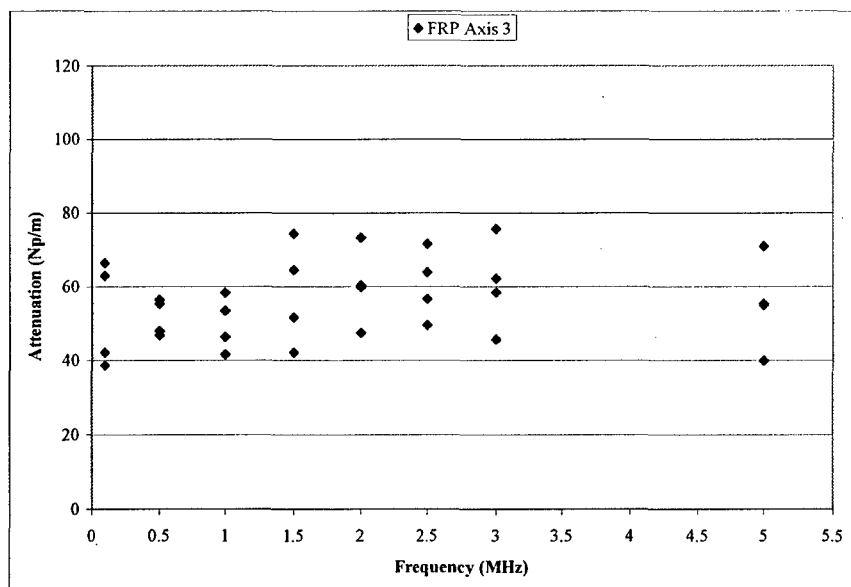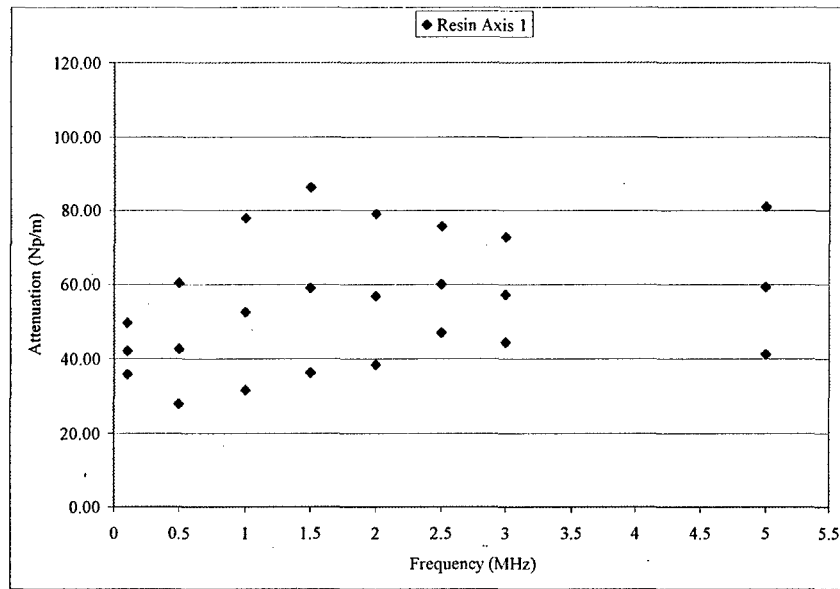
Fig. D. 23. Resin putty axis 1 attenuation. One cube each of three sizes allow for three attenuation calculations at each frequency. Data taken with PANAMETRICS-NDT™ EPOCH 4 flaw detector in through-transmission mode at 31.1 dB gain and K B-Aerotech, type Alpha, 5 MHz, 1.27 cm diameter, hard-faced transducers with water couplant.
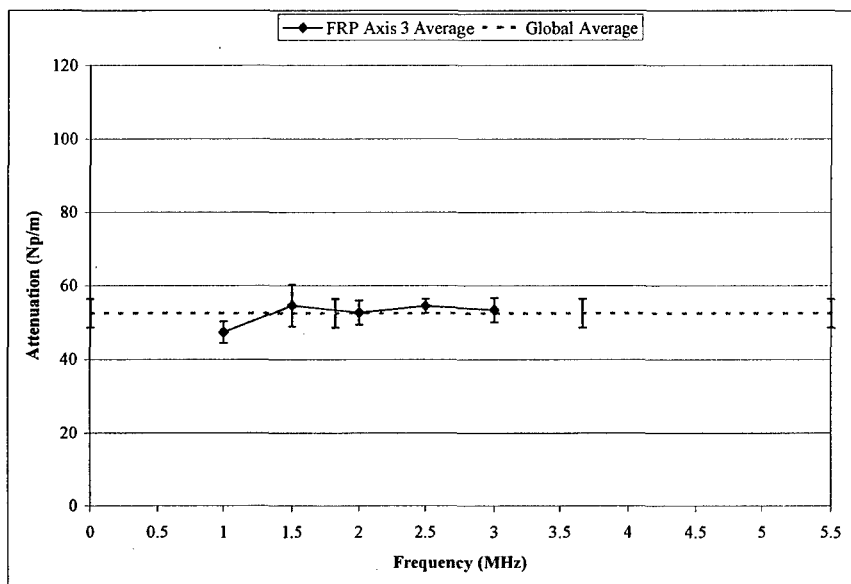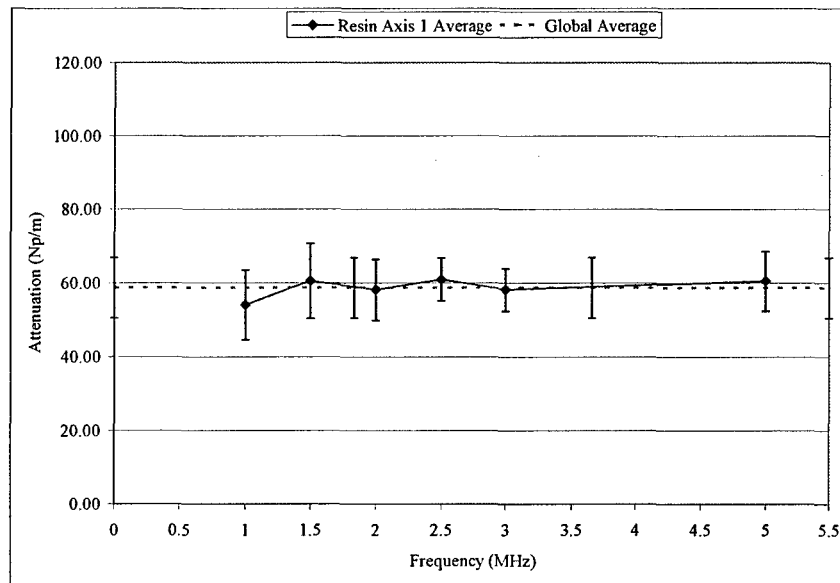

Fig. D. 24. Resin putty axis 1 attenuation average values. Points on the solid line represent the mean of three data points at that frequency. The height of the error bar represents one standard deviation for those three points. The dotted line and its error bars are the average and standard deviation of all data points in frequency range shown.

Table D. 3 summarizes the global average ultrasonic phase velocities and attenuations for all three materials. The standard deviation values in Table D. 3 are calculated with Eq. (D. 1) using all data points for each material.

Table D. 3. Global average ultrasonic phase velocity and attenuation measurements for all three materials.

Material	Global Average Ultrasonic Phase Velocity (m/s)	Velocity Standard Deviation (m/s)	Global Average Attenuation (Np/m)	Attenuation Standard Deviation (Np/m)
FRP Axis 1	2750	177	68.2	7.3
FRP Axis 2	3406	123	59.1	8.1
FRP Axis 3	3341	223	52.5	7.8
Syntactic Foam	2309	98	33.6	6.0
Resin Putty	2290	82	58.7	16.4

References

D-1   Kolsky, H. *Stress Waves in Solids* 2nd ed., p. 99-129. Dover Publications, New York (1963).

D-2   McClintock, F.A. and A.S. Argon. *Mechanical Behavior of Materials*, p. 33. Addison-Wesley, Reading (1966).

Page Intentionally Left Blank

Appendix E.   Input Signal Shape

Figure E. 1 shows the wave propagation as a function of depth and time in the three layers in an arrangement corresponding to the parameters in Table 4. For this combination of layer thicknesses and wave speeds, the first reflection from the second interface arrives back at the surface shortly after the second reflection from the first interface does. To a certain extent, the shape of the input signal can be adjusted in order to better discern these two signals.

Normalized Time, $tc_1/2l_1$
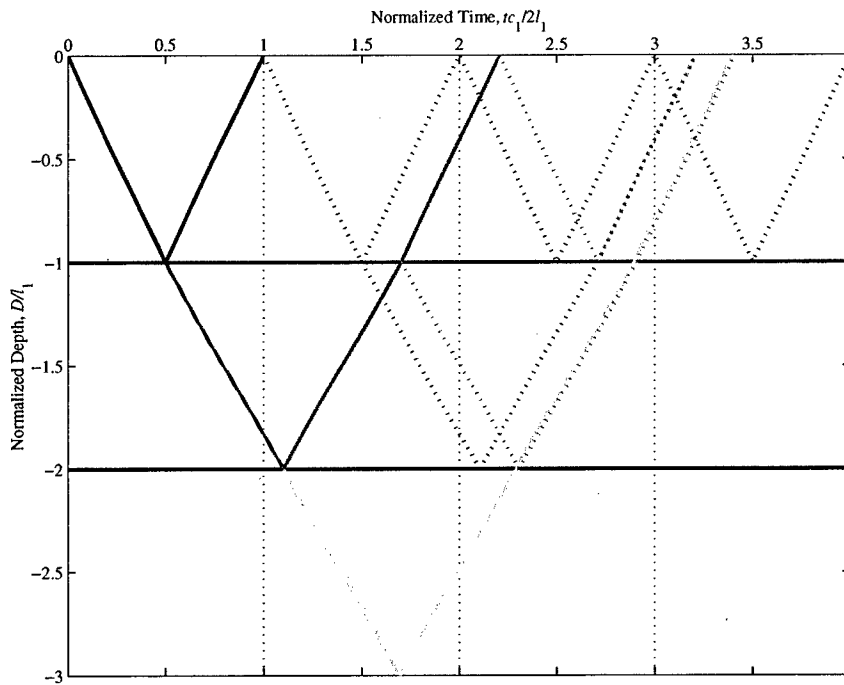
Fig. E. 1. Wave propagation in three layer composite with c_1=2750m/s, l_1=0.0127m, c_2/c_1=0.83, c_3/c_1=0.84, l_2/l_1=1.0, l_3/l_1=1.0. Only reflections that arrive back at surface at or before $tc_1/2l_1$=4 are shown.

The bandwidth of the input signal dictates the width (in the time domain) of the reflections seen at the surface. In this formulation, the bandwidth of the Gaussian-modulated cosinusoidal input function of Eq. (2) is represented by the non-dimensional parameter $\dfrac{f_\sigma}{f_c}$.

Since $\omega_\sigma = 2\pi f_\sigma = t_\sigma^{-1}$, a large value of $\dfrac{f_\sigma}{f_c}$ will result in a narrow signal in the time domain. The width of the input signal (and subsequent reflections) is assumed to extend six temporal standard deviations past the time of initiation of the signal. For a Gaussian envelope, this assures that the amplitude of the signal has decayed to 1.1 % of the peak.

This assumption is used with the arrival times of the reflections of concern to calculate a required bandwidth to separate the two signals. The second reflection from the first interface arrives at the surface at non-dimensional time

$$\frac{tc_1}{2l_1} = 2\left(\frac{l_1}{c_1} + \frac{l_1}{c_1}\right)\frac{c_1}{2l_1} = 2 \tag{E. 1}$$

The first reflection from the second interface arrives at the surface at non-dimensional time

$$\frac{tc_1}{2l_1} = 2\left(\frac{l_1}{c_1} + \frac{l_2}{c_2}\right)\frac{c_1}{2l_1} = 1 + \frac{l_2/l_1}{c_2/c_1} \tag{E. 2}$$

In order to separate these two signals, the width of the input signal must be less than the time interval between the two arrivals.

$$6t_\sigma \cdot \frac{c_1}{2l_1} < \left| -1 + \frac{l_2/l_1}{c_2/c_1} \right| \tag{E. 3}$$

The absolute value is used for the general case where $\dfrac{l_2/l_1}{c_2/c_1}$ can be greater than or equal to one.

Eq. (E. 3) can be re-written as

$$\frac{f_\sigma}{f_c} > \frac{1}{f_c} \cdot \frac{3}{\pi} \cdot \frac{c_1}{2l_1} \left| -1 + \frac{l_2/l_1}{c_2/c_1} \right|^{-1} \tag{E. 4}$$

Equation (E. 4) is only valid for the specific case of interference between the first reflection from the second interface and the second reflection from the first interface. The equivalent formulas for other scenarios can be derived in a similar fashion. Equation (D.4) is plotted for a range of central input frequencies in Fig. E. 2.
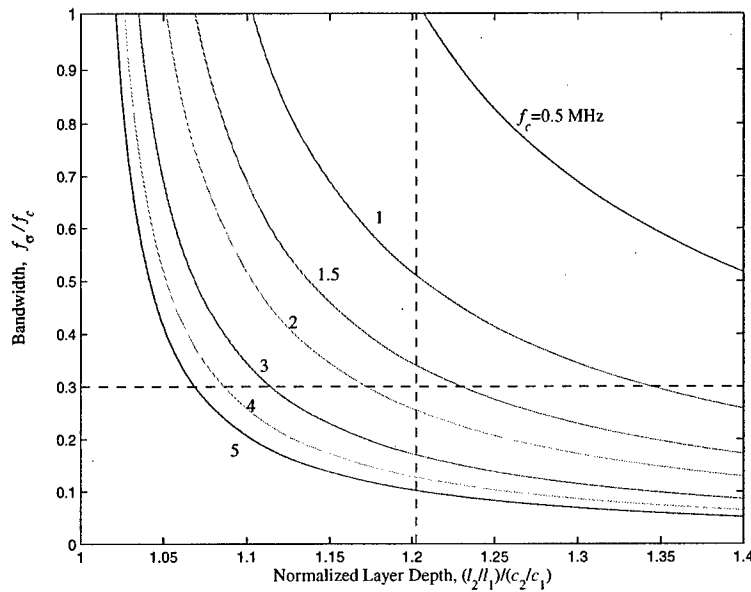
Fig. E. 2. Minimum bandwidth required to prevent overlap in first reflection from second interface and second reflection from first interface when c_1=2750 m/s and l_1=0.0127 m.

The dashed lines represent the configuration from Table 4. It can be seen that as $\dfrac{l_2/l_1}{c_2/c_1}$ approaches one, the required bandwidth asymptotically approaches infinity and it is impossible to isolate the overlapping reflections.

Page Intentionally Left Blank

Appendix F.   Complete Material Data

The complete set of data is included in Tables F. 1 through F. 5.

Material	Cube #	Nominal Size (in)	Axis	Measured Thickness (in)	Frequency (MHz)	Ultrasonic Measurement (in)	Measured Velocity (in/µs)	Amplitude (fraction of full screen)	Gain (dB)	Measured Velocity (m/s)	Calculated Attenuation (Np/m)
FRP	1	0.56	1	0.561	0.1	0.561	0.0995	0.49	31.1	2527	46
FRP	2	0.56	1	0.559	0.1	0.559	0.0997	0.42	31.1	2532	42
FRP	1	2	1	2.01	0.1	2.01	0.1135	0.09	31.1	2883	46
FRP	2	2	1	2.009	0.1	2.009	0.1138	0.09	31.1	2891	42
FRP	1	0.56	1	0.561	0.5	0.561	0.0999	0.50	31.1	2537	37
FRP	2	0.56	1	0.559	0.5	0.558	0.0988	0.60	31.1	2510	51
FRP	1	2	1	2.01	0.5	2.01	0.1134	0.09	31.1	2880	47
FRP	2	2	1	2.009	0.5	2.01	0.1136	0.13	31.1	2885	42
FRP	1	0.56	1	0.561	1	0.561	0.0999	0.91	31.1	2537	
FRP	2	0.56	1	0.559	1	0.559	0.0992	0.88	31.1	2520	54
FRP	1	2	1	2.01	1	2.01	0.1143	0.12	31.1	2903	55
FRP	2	2	1	2.009	1	2.008	0.1048	0.90	31.1		
FRP	1	0.56	1	0.561	1.5	0.561	0.1025	1.00	31.1	2604	65
FRP	2	0.56	1	0.559	1.5	0.559	0.1011	0.79	31.1	2568	75
FRP	1	2	1	2.01	1.5	2.01	0.1162	0.05	31.1	2951	81
FRP	2	2	1	2.009	1.5	2.008	0.1147	0.09	31.1	2913	59
FRP	1	0.56	1	0.561	2	0.561	0.1017	0.80	31.1	2583	66
FRP	2	0.56	1	0.559	2	0.561	0.1203	0.71	31.1		
FRP	1	2	1	2.01	2	2.01	0.1161	0.06	31.1	2949	70
FRP	2	2	1	2.009	2	2.009	0.1156	0.07	31.1	2936	
FRP	1	0.56	1	0.561	2.5	0.561	0.1031	0.67	31.1	2619	71
FRP	2	0.56	1	0.559	2.5	0.559	0.1024	0.62	31.1	2601	74
FRP	1	2	1	2.01	2.5	2.01	0.1154	0.04	31.1	2931	77
FRP	2	2	1	2.009	2.5	2.009	0.116	0.05	31.1	2946	68
FRP	1	0.56	1	0.561	3	0.561	0.1032	0.59	31.1	2621	67
FRP	2	0.56	1	0.559	3	0.559	0.1025	0.53	31.1	2604	70
FRP	1	2	1	2.01	3	2.01	0.116	0.04	31.1	2946	73
FRP	2	2	1	2.009	3	2.009	0.1163	0.05	31.1	2954	64
FRP	1	0.56	1	0.561	5	0.561	0.1036	0.35	31.1	2631	53
FRP	2	0.56	1	0.559	5	0.559	0.1031	0.34	31.1	2619	66
FRP	1	2	1	2.01	5	2.01	0.1166	0.03	31.1	2962	67
FRP	2	2	1	2.009	5	2.009	0.1161	0.05	31.1	2949	52

Table F. 1. Complete ultrasonic phase velocity and attenuation data for FRP axis 1. Shaded rows represent outlier data points not used in analysis. Data taken with PANAMETRICS-NDT™ EPOCH 4 flaw detector in through-transmission mode and K B-Aerotech, type Alpha, 5 MHz, 1.27 cm diameter, hard-faced transducers with water couplant.

Material	Cube #	Nominal Size (in)	Axis	Measured Thickness (in)	Frequency (MHz)	Ultrasonic Measurement (in)	Measured Velocity (in/μs)	Amplitude (fraction of full screen)	Gain (dB)	Measured Velocity (m/s)	Calculated Attenuation (Np/m)
FRP	1	0.56	2	0.534	0.1	0.534	0.1195	0.63	31.1	3035	67
FRP	2	0.56	2	0.53	0.1	0.53	0.1252	0.79	31.1	3180	58
FRP	1	2	2	2.012	0.1	2.012	0.1439	0.09	31.1	3655	52
FRP	2	2 ·	2	1.91	0.1	1.91	0.1444	0.06	31.1	3668	74
FRP	1	0.56	2	0.534	0.5	0.534	0.1185	0.56	31.1	3010	42
FRP	2	0.56	2	0.53	0.5	0.531	0.1261	1.00	31.1	3203	43
FRP	1	2	2	2.012	0.5	2.012	0.1348	0.20	31.1	3424	27
FRP	2	2	2	1.91	0.5	1.91	0.1349	0.13	31.1	3426	58
FRP	1	0.56	2	0.534	1	0.534	0.1227	0.81	31.1	3117	52
FRP	2	0.56	2	0.53	1	0.53	0.1319	1.00	31.1	3350	44
FRP	1	2	2	2.012	1	2.012	0.1364	0.19	31.1	3465	39
FRP	2	2	2	1.91	1	1.91	0.1348	0.13	31.1	3424	58
FRP	1	0.56	2	0.534	1.5	0.534	0.1229	0.75	31.1	3122	50
FRP	2	0.56	2	0.53	1.5	0.53	0.1317	1.00	31.1	3345	49
FRP	1	2	2	2.012	1.5	2.012	0.1371	0.16	31.1	3482	41
FRP	2	2	2	1.91	1.5	1.91	0.1365	0.13	31.1	3467	58
FRP	1	0.56	2	0.534	2	0.534	0.1238	0.53	31.1	3145	51 ·
FRP	2	0.56	2	0.53	2	0.529	0.131	0.89	31.1	3327	58
FRP	1	2	2	2.012	2	2.012	0.1385	0.10	31.1	3518	44
FRP	2	2	2	1.91	2	1.911	0.1376	0.09	31.1	3495	65
FRP	1	0.56	2	0.534	2.5	0.534	0.1248	0.47	31.1	3170	54
FRP	2	0.56	2	0.53	2.5	0.53	0.1309	0.71	31.1	3325	55
FRP	1	2	2	2.012	2.5	2.012	0.1382	0.09	31.1	3510	44
FRP	2	2	2	1.91	2.5	1.91	0.1375	0.07	31.1	3493	· 66
FRP	1	0.56	2	0.534	3	0.534	0.1259	0.40	31.1	3198	59
FRP	2	0.56	2	0.53	3	0.53	0.1318	0.56	31.1	3348	59
FRP	1	2	2	2.012	3	2.012	0.1393	0.06	31.1	3538	51
FRP	2	2	2	1.91	3	1.911	0.1381	0.05	31.1	3508	69
FRP	1	0.56	2	0.534	5	0.534	0.1276	0.24	31.1	3241	45
FRP	2	0.56	2	0.53	5	0.53	0.133	0.35	31.1	3378	58
FRP	1	2	2	2.012	5	2.012	0.1401	0.04	31.1	3559	48
FRP	2	2	2	1.91	5	1.91	0.1377	0.05	31.1	3498	56

Table F. 2. Complete ultrasonic phase velocity and attenuation data for FRP axis 2. Shaded rows represent outlier data points not used in analysis. Data taken with PANAMETRICS-NDT™ EPOCH 4 flaw detector in through-transmission mode and K B-Aerotech, type Alpha, 5 MHz, 1.27 cm diameter, hard-faced transducers with water couplant.

Material	Cube #	Nominal Size (in)	Axis	Measured Thickness (in)	Frequency (MHz)	Ultrasonic Measurement (in)	Measured Velocity (in/μs)	Amplitude (fraction of full screen)	Gain (dB)	Measured Velocity (m/s)	Calculated Attenuation (Np/m)
FRP	1	0.56	3	0.526	0.1	0.526	0.126	0.74	31.1	3200	42
FRP	2	0.56	3	0.535	0.1	0.535	0.1189	0.64	31.1	3020	63
FRP	1	2	3	2.015	0.1	2.015	0.144	0.06	31.1	3658	66
FRP	2	2	3	2.082	0.1	2.082	0.1487	0.14	31.1	3777	39
FRP	1	0.56	3	0.526	0.5	0.526	0.1246	0.93	31.1	3165	48
FRP	2	0.56	3	0.535	0.5	0.534	0.1169	0.88	31.1	2969	55
FRP	1	2	3	2.015	0.5	2.015	0.1348	0.11	31.1	3424	56
FRP	2	2	3	2.082	0.5	2.083	0.1376	0.14	31.1	3495	47
FRP	1	0.56	3	0.526	1	0.526	0.1313	1.00	31.1	3335	46
FRP	2	0.56	3	0.535	1	0.535	0.1217	0.82	31.1	3091	53
FRP	1	2	3	2.015	1	2.015	0.1364	0.11	31.1	3465	58
FRP	2	2	3	2.082	1	2.082	0.1367	0.16	31.1	3472	42
FRP	1	0.56	3	0.526	1.5	0.526	0.1319	1.00	31.1	3350	52
FRP	2	0.56	3	0.535	1.5	0.535	0.1243	0.68	31.1	3157	65
FRP	1	2	3	2.015	1.5	2.015	0.1375	0.06	31.1	3493	74
FRP	2	2	3	2.082	1.5	2.082	0.1406	0.13	31.1	3571	42
FRP	1	0.56	3	0.526	2	0.526	0.1304	0.96	31.1	3312	60
FRP	2	0.56	3	0.535	2	0.534	0.1251	0.58	31.1	3178	60
FRP	1	2	3	2.015	2	2.015	0.1388	0.06	31.1	3526	73
FRP	2	2	3	2.082	2	2.082	0.1386	0.09	31.1	3520	47
FRP	1	0.56	3	0.526	2.5	0.526	0.1317	0.75	31.1	3345	64
FRP	2	0.56	3	0.535	2.5	0.535	0.1269	0.42	31.1	3223	57
FRP	1	2	3	2.015	2.5	2.015	0.1384	0.05	31.1	3515	72
FRP	2	2	3	2.082	2.5	2.082	0.1406	0.06	31.1	3571	50
FRP	1	0.56	3	0.526	3	0.526	0.1313	0.70	31.1	3335	62
FRP	2	0.56	3	0.535	3	0.535	0.1267	0.36	31.1	3218	58
FRP	1	2	3	2.015	3	2.015	0.1396	0.04	31.1	3546	76
FRP	2	2	3	2.082	3	2.082	0.1412	0.06	31.1	3586	46
FRP	1	0.56	3	0.526	5	0.526	0.1322	0.44	31.1	3358	55
FRP	2	0.56	3	0.535	5	0.535	0.1282	0.24	31.1	3256	55
FRP	1	2	3	2.015	5	2.015	0.1401	0.03	31.1	3559	71
FRP	2	2	3	2.082	5	2.082	0.141	0.05	31.1	3581	40

Table F. 3. Complete ultrasonic phase velocity and attenuation data for FRP axis 3. Shaded rows represent outlier data points not used in analysis. Data taken with PANAMETRICS-NDT™ EPOCH 4 flaw detector in through-transmission mode and K B-Aerotech, type Alpha, 5 MHz, 1.27 cm diameter, hard-faced transducers with water couplant.

Material	Cube #	Nominal Size (in)	Axis	Measured Thickness (in)	Frequency (MHz)	Ultrasonic Measurement (in)	Measured Velocity (in/μs)	Amplitude (fraction of full screen)	Gain (dB)	Measured Velocity (m/s)	Calculated Attenuation (Np/m)
Foam	1	1	1	0.983	0.1	0.983	0.0867	0.38	31.1	2202	21.43
Foam	1	2	1	1.987	0.1	1.987	0.0906	0.22	31.1	2301	57.98
Foam	1	3	1	2.993	0.1	2.994	0.0962	0.05	31.1	2443	39.73
Foam	1	1	1	0.983	0.5	0.984	0.0867	0.42	31.1	2202	25.36
Foam	1	2	1	1.987	0.5	1.988	0.0907	0.22	31.1	2304	57.98
Foam	1	3	1	2.993	0.5	2.994	0.0933	0.05	31.1	2370	41.69
Foam	1	1	1	0.983	1	0.983	0.0865	0.50	31.1	2197	27.18
Foam	1	2	1	1.987	1	1.988	0.0904	0.25	31.1	2296	35.86
Foam	1	3	1	2.993	1	2.992	0.0961	0.10	31.1	2441	31.52
Foam	1	1	1	0.983	1.5	0.983	0.0866	0.60	31.1	2200	35.93
Foam	1	2	1	1.987	1.5	1.987	0.0906	0.24	31.1	2301	27.13
Foam	1	3	1	2.993	1.5	2.991	0.0959	0.12	31.1	2436	31.52
Foam	1	1	1	0.983	2	0.982	0.0866	0.56	31.1	2200	40.37
Foam	1	2	1	1.987	2	1.988	0.0908	0.20	31.1	2306	27.13
Foam	1	3	1	2.993	2	2.993	0.0961	0.10	31.1	2441	33.74
Foam	1	1	1	0.983	2.5	0.983	0.0869	0.50	31.1	2207	42.30
Foam	1	2	1	1.987	2.5	1.986	0.0906	0.17	31.1	2301	24.89
Foam	1	3	1	2.993	2.5	2.993	0.0966	0.09	31.1	2454	33.59
Foam	1	1	1	0.983	3	0.983	0.0869	0.45	31.1	2207	43.08
Foam	1	2	1	1.987	3	1.988	0.0909	0.15	31.1	2309	24.60
Foam	1	3	1	2.993	3	2.993	0.0966	0.08	31.1	2454	33.83
Foam	1	1	1	0.983	5	0.983	0.0871	0.34	31.1	2212	44.25
Foam	1	2	1	1.987	5	1.988	0.0909	0.11	31.1	2309	30.86
Foam	1	3	1	2.993	5	2.993	0.0965	0.05	31.1	2451	37.55

Table F. 4. Complete ultrasonic phase velocity and attenuation data for syntactic foam axis 1. Shaded rows represent outlier data points not used in analysis. Data taken with PANAMETRICS-NDT™ EPOCH 4 flaw detector in through-transmission mode and K B-Aerotech, type Alpha, 5 MHz, 1.27 cm diameter, hard-faced transducers with water couplant.

Material	Cube #	Nominal Size (in)	Axis	Measured Thickness (in)	Frequency (MHz)	Ultrasonic Measurement (in)	Measured Velocity (in/μs)	Amplitude (fraction of full screen)	Gain (dB)	Measured Velocity (m/s)	Calculated Attenuation (Np/m)
Resin	1	1	1	1.042	0.1	1.041	0.0862	0.39	31.1	2189	35.86
Resin	2	2	1	2.091	0.1	2.092	0.0908	0.15	31.1	2306	49.66
Resin	3	3	1	2.962	0.1	2.962		0.05	31.1	0	42.12
Resin	1	1	1	1.042	0.5	1.042	0.0864	0.40	31.1	2195	27.94
Resin	2	2	1	2.091	0.5	2.092	0.0901	0.19	31.1	2289	60.34
Resin	3	3	1	2.962	0.5	2.96	0.0934	0.05	31.1	2372	42.64
Resin	1	1	1	1.042	1	1.042	0.0854	0.65	31.1	2169	31.61
Resin	2	2	1	2.091	1	2.09	0.0902	0.28	31.1	2291	77.87
Resin	3	3	1	2.962	1	2.961	0.0943	0.05	31.1	2395	52.59
Resin	1	1	1	1.042	1.5	1.041	0.0862	0.71	31.1	2189	36.29
Resin	2	2	1	2.091	1.5	2.091	0.0906	0.27	31.1	2301	86.31
Resin	3	3	1	2.962	1.5	2.962	0.0948	0.04	31.1	2408	58.98
Resin	1	1	1	1.042	2	1.041	0.0866	0.64	31.1	2200	38.41
Resin	2	2	1	2.091	2	2.092	0.0908	0.23	31.1	2306	79.07
Resin	3	3	1	2.962	2	2.964	0.0951	0.04	31.1	2416	56.85
Resin	1	1	1	1.042	2.5	1.042	0.0868	0.56	31.1	2205	47.02
Resin	2	2	1	2.091	2.5	2.091	0.0911	0.16	31.1	2314	75.67
Resin	3	3	1	2.962	2.5	2.963	0.0945	0.03	31.1	2400	60.01
Resin	1	1	1	1.042	3	1.042	0.087	0.49	31.1	2210	44.43
Resin	2	2	1	2.091	3	2.092	0.0909	0.15	31.1	2309	72.75
Resin	3	3	1	2.962	3	2.961	0.0945	0.03	31.1	2400	57.28
Resin	1	1	1	1.042	5	1.041	0.087	0.36	31.1	2210	41.23
Resin	2	2	1	2.091	5	2.092	0.0909	0.12	31.1	2309	80.99
Resin	3	3	1	2.962	5	2.963	0.0826	0.02	31.1	2098	59.27

Table F. 5. Complete ultrasonic phase velocity and attenuation data for resin putty axis 1. Shaded rows represent outlier data points not used in analysis. Data taken with PANAMETRICS-NDT™ EPOCH 4 flaw detector in through-transmission mode and K B-Aerotech, type Alpha, 5 MHz, 1.27 cm diameter, hard-faced transducers with water couplant.